

Mechanochemical Solid Form Screening of Zeolitic Imidazolate Frameworks using Structure-Directing Liquid Additives

Ivana Brekalo,^{a,b,c,*} Katarina Lisac,^a Joseph R. Ramirez,^b Petra Pongrac,^{a,d} Yizhi Xu,^e Michael Ferguson,^f Joseph M. Marrett,^f Mihails Arhangelis, ^{e,*} Tomislav Friščić,^{e,f,*} K. Travis Holman^{b,*}

^aDivision of Physical Chemistry, Ruđer Bošković Institute, Zagreb, Croatia

^bDepartment of Chemistry, Georgetown University, Washington, D.C., USA

^cDepartment of Chemistry, McGill University, Montréal, Canada

^dFaculty of Chemical Engineering and Technology, University of Zagreb, Zagreb, Croatia

^eFaculty of Chemistry, University of Warsaw, Warsaw, Poland

^fSchool of Chemistry, University of Birmingham, Birmingham, UK

KEYWORDS: *Templation, mechanochemistry, zeolitic imidazolate frameworks, periodic DFT, additives*

ABSTRACT: We demonstrate a systematic application of the mechanochemical liquid-assisted grinding (LAG) methodology to screen for forms of zinc imidazolate (ZnIm_2), of fundamental importance as the simplest member of the zeolitic imidazolate framework materials family. The exploration of 45 different liquid additives, selected based on their molecular structure and physicochemical properties has resulted in seven different ZnIm_2 topologies, appearing in 12 structurally distinct solid forms (including two previously unknown forms of the **crb** (BCT) topology), amorphous phases, and the interrupted **moc** topology material. All prepared topologies were also explored computationally, using dispersion-corrected periodic density functional theory (DFT) calculations, enabling the rationalization of screening outcomes, and setting the stage for future prediction of additive-directed MOF synthesis. This first systematic exploration of LAG in screening for three-dimensional metal-organic frameworks demonstrates the potential of the liquid additive to not only accelerate materials synthesis, but also to direct it towards topologically different frameworks. The ability to discover novel forms in a material that already exhibits at least 21 crystallographically and functionally different forms provides a strong testimony on the power of mechanochemistry in metal-organic materials discovery.

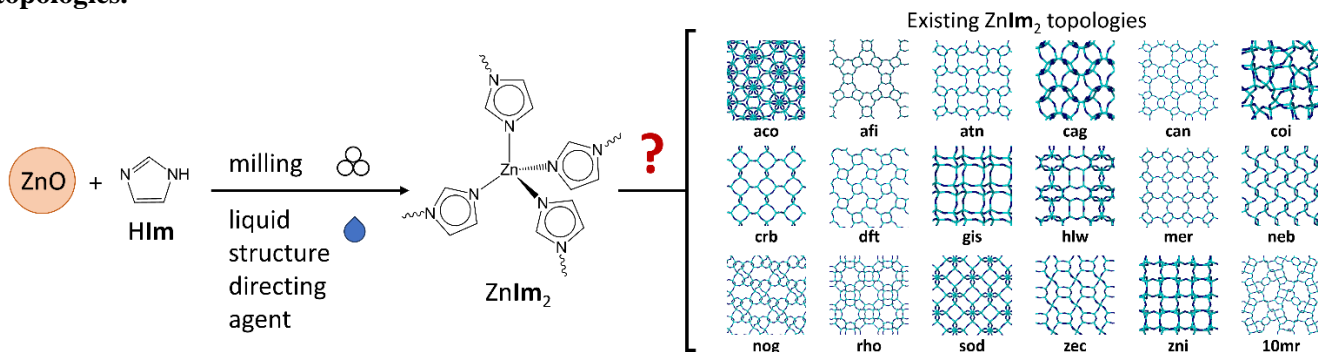
1. Introduction

The physicochemical properties of materials are intimately linked with their structure, so form screening is a crucial aspect of solid-state materials science. For example, solid form screening in the pharmaceutical industry is prevalent, as it is well recognized that different solid forms of active pharmaceutical ingredients can offer different performance properties, such as solubility, stability, dissolution rates or bioavailability.¹⁻⁴ Similarly, the properties of porous materials are highly dependent on the size, shape, and chemical compositions of their pores and pore windows.⁵⁻⁸ Significant effort has thus been dedicated to the rational design of metal-organic frameworks (MOFs) with advanced properties (such as microporosity, conductivity, or adsorbent selectivity) by engineering their structures.⁹⁻¹⁶ A particular challenge is the control of polymorphism, where the same starting materials can give many different products, the most porous of which are inherently metastable with respect to their less porous or non-porous polymorphs, often resulting in MOF flexibility¹⁷⁻²⁰ and form conversion²¹⁻²³. Recent years have thus seen increasing focus on the fundamental understanding of structure-directing effects and stability in MOFs.^{13,24-26}

Zeolitic imidazolate frameworks (ZIFs)²⁷⁻³¹ – a class of MOFs built from tetrahedral metal centers (e.g. Zn^{2+} , Cd^{2+} , Co^{2+}) and imidazolate ligands – are particularly susceptible to polymorphism and form diversity. Like zeolites, ZIFs can exist in many topological forms. For example, the sterically unhindered zinc imidazolate (ZnIm_2), is known to exist in at least 18 topologies³² (Scheme 1), some of which can take several distinct crystallographic/ conformational forms. For example, the **crb**- ZnIm_2 ^{33,34} exists in three different forms^{27,35} with different space groups, unit cell volumes, and predicted pore properties (Table 1, Table S9). Preparations of ZnIm_2 often yield (pseudo)polymorphic mixtures, and some topological forms (e.g. **mer**, **gis**) have, to the best of

our knowledge, only ever been reported in one experiment each, isolated as single crystals.²⁷ Amorphous forms of ZnIm_2 have also been prepared,^{36–38} as has an interrupted dense framework of the **moc** topology (**moc**- $\text{Zn}_4\text{Im}_8(\text{HIm})$).^{39,40} Overall, ZIF syntheses broadly, and ZnIm_2 synthesis in particular, pose a significant challenge in terms of solid form control and the stabilization of certain porous forms.

Scheme 1. The use of liquid-directed mechanochemical screening in the preparation of zinc imidazolate topologies.



Solid form control strategies used on ZIFs derived from substituted imidazoles, such as the use of specific linkers,^{31,41} mixed linkers,³⁵ and the steric index approach⁴² unfortunately cannot be applied to unsubstituted MIm_2 ZIFs. Instead, solid form control is often achieved using putative templates, such as amide solvents,^{43–46} structure-directing agents,⁴⁷ or macrocycles⁴⁸. This often involves time- and energy-intensive solvothermal screening, which inherently limits the template scope to molecules that are miscible with/soluble in the solvents used. In that context, the development of methodologies for sustainable, efficient MOF solid form screening is very important, but has remained largely unexplored, especially in comparison with the wide, continuously growing set of methodologies being deployed in pharmaceutical materials science. In particular, mechanochemical ball milling techniques,⁴⁹ especially those involving a liquid additive (liquid-assisted grinding, LAG) have been demonstrated as highly efficient for rapid discovery of new forms of organic solids, such as polymorphs, cocrystals, salts and more,^{50–52} including sustainably⁵³ at a large scale.^{54,55}

Here we demonstrate the first systematic exploration of liquid additives for the mechanochemical solid form screening of the simplest and most polymorphic ZIF representative, zinc imidazolate. We show that this fast, effective and environmentally friendly screening approach can provide 13 different crystalline ZIF frameworks, including two new forms of the **crb** (BCT) topology, as well as amorphous solid forms. Application of previously validated periodic density functional theory (DFT) computational methods⁵⁶ to the solvated ZnIm_2 systems reveals that, while kinetic effects can play a significant role, ultimately the topological outcomes of LAG ZnIm_2 syntheses are ultimately governed by the thermodynamic stabilities of the specific solvated ZnIm_2 structures. We anticipate that this solid form screening method can be widely applied to discover and control the polymorphism of different classes of host-guest materials.

2. Results and discussion

2.1. General outcomes of LAG screening. Mechanochemistry has been shown to be a highly versatile approach to synthesize a diverse range of coordination compounds, encompassing discrete complexes, as well as coordination polymers of different dimensionality, including MOFs.^{57–61} Moreover, mechanochemical synthesis of ZIFs has been explored, including neat grinding (NG) syntheses,⁶² LAG/ILAG (ion-and-liquid assisted grinding)⁶³ and aging syntheses,^{64–66} *in situ* and *ex situ* monitoring,^{67–71} discovery of new ZIF topologies through mechanochemistry,⁷² and scale-up.^{54,73,74} Furthermore, periodic density functional theory (DFT) calculations have been used to explain mechanochemical reactivity,^{56,75} and even predict the crystal structures of the products of milling syntheses.^{76,77} Despite this extensive body of research, the role of liquid additives in the mechanochemical syntheses of MOFs, and their potential utility as stabilizers, structure-directing agents, and even presumptive templates in MOF solid form screening has never been systematically studied.

Inspired by the zeolite community's use of cationic templates in the controlled synthesis of desired zeolite topologies, and our own work on the solvothermal templation of **mer**- ZnIm_2 ,⁴⁸ we have previously used the macrocyclic Cram's cavitands⁷⁸ for targeted mechanochemical synthesis of **rho**- ZnIm_2 .^{79,80} Certain cavitands were highly successful at templating the *double-8-ring* (*d8r*) motif of the **rho** topology *via* eight (imidazolate) C-H...O (cavitand) hydrogen bonds, enabling the synthesis of decagram quantities of a highly porous **rho**- ZnIm_2

material in quantitative yield, without bulk solvent. However, the cavitated template molecules themselves are not ubiquitous, require solvothermal organic synthesis and purification, and most importantly, they template only one specific topological motif – the *d8r*. We are now seeking presumptive templates that would be readily available, and able to direct the synthesis of many different solid forms of ZIFs in a fast and efficient mechanochemical screening. One possible avenue is the use of small-molecule liquids as structure-directing agents. The role of liquid additives in mechanochemistry is still not fully resolved, but they are known to assist and accelerate mechanochemical syntheses, while sometimes also directing the synthetic outcome,⁸¹ including in coordination polymers,⁸² MOFs,^{83,84} and ZIFs.⁶³ We therefore propose that the use of small molecule liquid additives as presumptive templates and stabilizing pore-fillers will provide an avenue for such screening.

We selected 45 different liquids to serve as additives in the mechanochemical reactions of zinc oxide and imidazole (**HI**m). The liquids were chosen to sample a range of properties, including polarity, aromaticity, proticity, functional groups, molecular shapes and sizes, etc. The use of mechanochemistry enabled a very broad additive scope, as solubility of the reagents is not a limiting factor. For example, we can use highly nonpolar liquids such as cyclohexane (cHANE) in conjunction with the ionic ZnO and the highly polar and protic imidazole. The full list of liquid additives explored can be found in SI-1.7. (Table S1). The screening was conducted by adding a set amount of liquid (100 μ L, unless otherwise noted; $\eta = 0.5 \mu$ L/mg) into a milling jar containing two milling balls and a 1:2 stoichiometric ratio of zinc oxide (ZnO) and imidazole (total mass = 200 mg), and then milling the mixture at a frequency of 30 Hz for 15, 30, 60, or 90 minutes. Neat grinding control experiments (without the addition of liquid additives) were also performed. The milled product mixtures were then analyzed by powder X-ray diffraction (PXRD), and the topologic outcome of the synthesis determined by comparison to an internal database of simulated PXRD patterns of different ZIF forms, whose structures were extracted from the Cambridge Structural Database (CSD).⁸⁵ For selected liquid additives, different experimental conditions were tested (using steel or Teflon™ milling jars, different amounts of liquid, different milling times, aging the reaction mixture at room temperature).

The screening results (section SI-2.1.45, summarized in tables S3 and S4) can be classified into three main outcomes (Figure 1): 1) the liquid additive yields a pure **ZnIm**₂ product of a single topology; 2) the liquid additive yields a mixture of different **ZnIm**₂ topologies; or 3) the topological outcome changes depending on experimental conditions. In most cases, the resulting framework materials presumably encapsulate the used additives as guests, and will be named *x*guest@**top**-**ZnIm**₂, where **top** designates the topology and form of the product, and *x* the number of included guest molecules per Zn. For example, reactions with added cyclohexanone (cHONE) always yielded 0.5cHONE@**neb1**-**ZnIm**₂; the cHONE solvate of form 1 of the **neb**-topology zinc imidazolate (hereafter named **neb1**, compares to 0.5MORPH@**neb1**-**ZnIm**₂, CSD code KUDJOK⁸⁶, where MORPH = morpholine), regardless of milling time or milling vessel material (Figure 1b, Figure S8). Conversely, milling with acetonitrile (MeCN) provides a mixture of **coi**-**ZnIm**₂ (compares to CSD code IMIDZB07⁸⁷) and **zni**-**ZnIm**₂ (compares to CSD code IMIDZB07⁸⁷ in varying ratios depending on the reaction conditions (Figure 1c, Figure S24), but never as a single pure phase. The most common case is 3), where the templation outcome partially depends on the reaction conditions. Different conditions can result in different pure phases for the same liquid additive. For example, using cHANE as the structure-directing agent gives 0.5cHANE@**cag**-**ZnIm**₂ (compares to 0.5DMF@**cag**-**ZnIm**₂, CSD code VEJYUF01,⁴⁷ DMF = N,N-dimethylformamide) after 15 min of milling in a Teflon™ jar, but yields 0.5cHANE@**neb1**-**ZnIm**₂ upon longer milling (≥ 30 min) in a Teflon™ jar, or milling in a steel jar (Figure 1d, Figure S5). Such changes in topology upon different milling periods were also previously reported in *in situ* studies of ZIF syntheses using substituted imidazoles.^{71,72} On the other hand, changing the conditions sometimes switches between pure and mixed phases. A 15 minute milling reaction using pyridine (PYR) results in a mixture of *x*PYR@**crb1**-**ZnIm**₂ (compares to 1.5DMF@**crb1**-**ZnIm**₂ CSD code VEJYIT²⁷) and 0.5PYR@**neb2**-**ZnIm**₂ (CSD code KEVLEE⁸⁸) phases, while milling for an hour provides pure 0.5PYR@**neb2**-**ZnIm**₂ (Figure S42).

Overall, the presented fast and accessible screening method resulted in pure samples of seven different **ZnIm**₂ topologies – namely **zni**,⁸⁷ **coi**,⁸⁷ **crb**,^{27,35} **cag**,⁴⁷ **neb**,^{86,88} **nog**,⁴⁷ and **10mr**⁴³ – out of the 18 known **ZnIm**₂ topologies, as well as the **moc**³⁹ interrupted framework, and amorphous phases (Figure 2). Importantly, this screening also revealed two new, crystallographically distinct forms of **crb**-**ZnIm**₂, along with providing the three already known **crb**-**ZnIm**₂ phases (pure or in mixture), as well as the two known phases of **neb**-**ZnIm**₂. Altogether, 13 distinct crystalline frameworks based on zinc imidazolate have thus been found *via* our screening method (Figure 1). Many of these exist in several solvated forms, encapsulating different guest molecules, providing even more distinct materials. The PXRD analyses and summaries of the topological outcomes of all

reactions can be found in the Supplementary Information (SI-2.1.), while herein we discuss only the observed trends, new forms, and selected interesting cases.

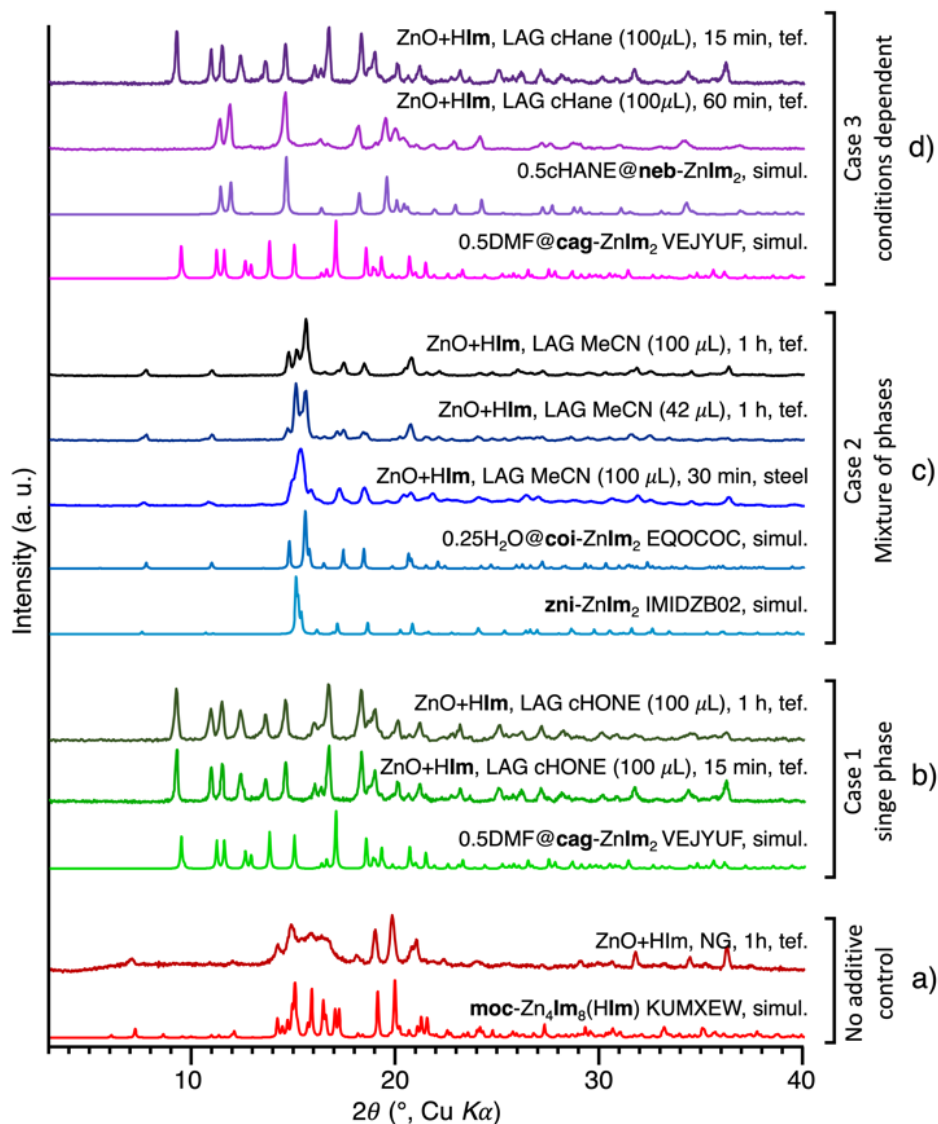


Figure 1. PXRD patterns representing the results of milling ZnO and imidazole a) without additive, b) with added cyclohexanone (cHONE), c) with added acetonitrile (MeCN), d) with added cyclohexane (cHANE). Tef = Teflon™ jar, simul.= simulated

2.2. Preparation of dense forms. The most commonly observed phases in the screening were, expectedly, the highest density forms (densities between 1.5 and 1.6 g/cm³): **moc-Zn₄Im₈HIm** (3/45 liquids + NG, void fraction 0.1%), **zni-ZnIm₂** (10/45 liquids, void fraction 1.3%) and **coi-ZnIm₂** (10/45 liquids, void fraction 1.1%). **moc-Zn₄Im₈HIm**, an interrupted dense framework of the **moc** topology, where one quarter of the **Im**⁻ linkers are replaced with an [**Im**···H···**Im**]⁻ unit, is also the predominant product of the control NG reactions, in both steel and Teflon™ jars, after 15, 30, or 60 min of milling. Only the 60 min milling reaction in a steel jar provides **zni-ZnIm₂** alongside **moc-Zn₄(Im)₈HIm**. The **moc**, **zni** and **coi** phases also appear as products of heating or washing of the less dense phases (Figure S38), or after long periods of room temperature (RT) aging (Figures S12, S44), hinting at their higher thermodynamic stability compared to the more open phases. Traditionally, the **moc**, **zni** and **coi** phases have mostly been synthesized from ionic liquids,³⁹ thermally in the solid state,⁴⁰ or by conversion from more open forms.⁸⁸

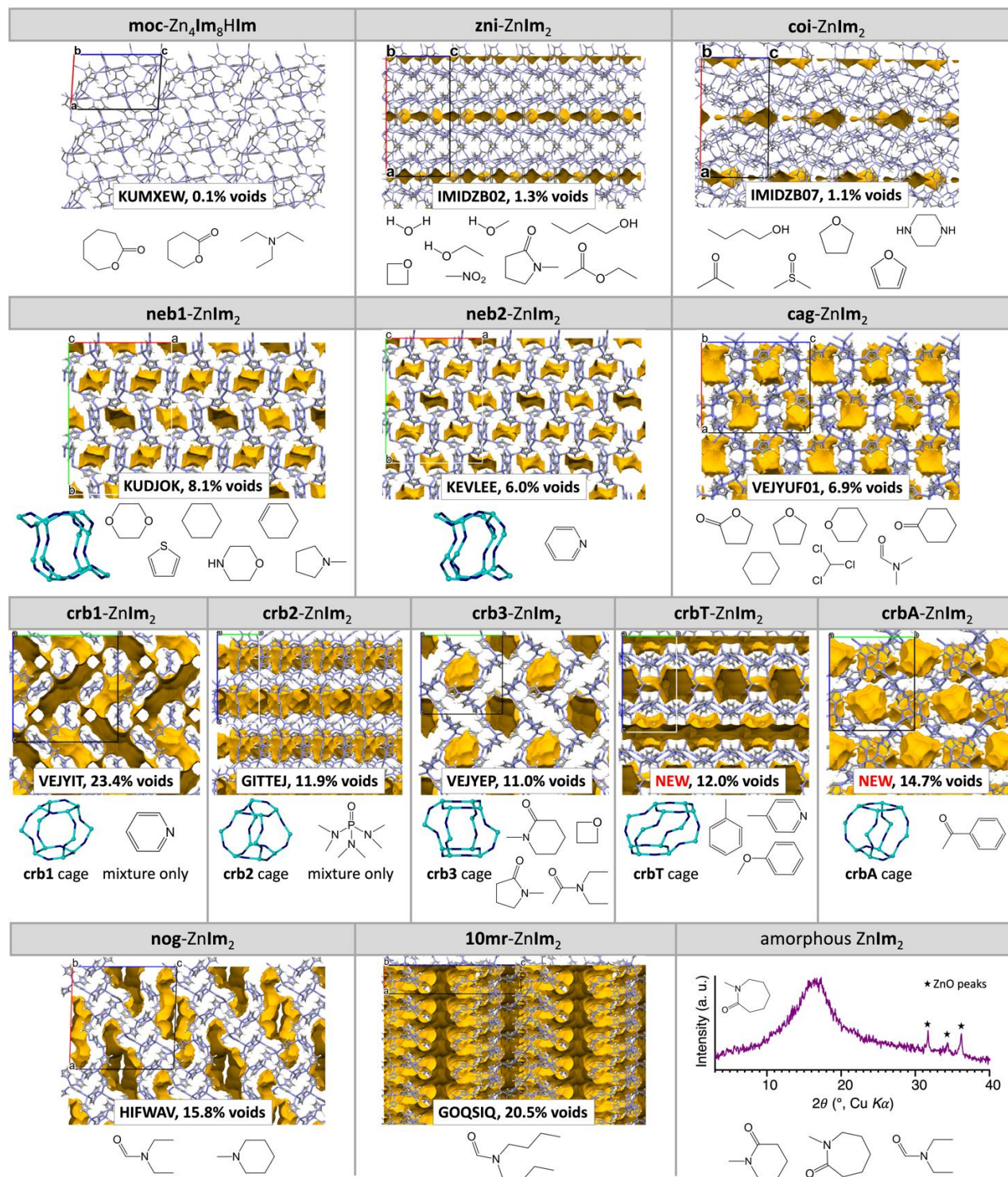


Figure 2. Overview of the topological results of LAG screening. The crystal structures of different topological forms obtained by LAG mechanochemical screening are shown in the capped sticks representations, along with their CSD code (if applicable), void percentage (calculated using the solvent accessible surface in Mercury, 1.2 Å probe), and the additive used to synthesize them as pure phases. Node-and-linker representations of the building block cages for the crb forms are also shown (light blue = Zn, dark blue = Im⁻ centroid). Solvent accessible surfaces are shown in yellow contour.

Together, this leads us to conclude that these are the thermodynamically preferred structures when no effective pore-filling guest is available to stabilize a more open ZnIm₂ topology. Any selectivity towards generating these structures in the presence of liquid additives is therefore likely due to surface processes, or transient templation

effects in the early stages of ZIF nucleation, where the liquid may act as a temporary template and then leave the structure. In the LAG screening, protic liquids (H₂O, MeOH, EtOH) seem to steer the reaction to **zni-ZnIm₂**, while polar aprotic liquids (acetone (AcMe), dimethylsulfoxide (DMSO), tetrahydrofuran (THF)) favor **coi-ZnIm₂**. These two phases also appear as mixtures concomitantly with certain liquid templates (ethylene glycol (EtGly), H₂O, MeCN), which is unsurprising since they have been otherwise shown to interconvert under different pressures and temperatures.^{87,88}

2.3. Lower density forms of ZnIm₂. The next most prevalent ZnIm₂ topologies to appear in the screening are **cag** (7/45 liquids, void fraction 6.9%) and **neb** (7/45, void fraction 8.1% for **neb1** and 6.0% for **neb2**), which have theoretical activated densities between 1.0 and 1.3 g/cm³. These both predominantly appear using aliphatic cyclic molecules with 5- or 6-membered rings as additives and structure-directing agents. **cag-ZnIm₂** appears to be preferred with more polar molecules (e.g. tetrahydropyran (THP), cHONE, THF), while **neb-ZnIm₂** materials appear mostly using nonpolar and nitrogen-containing additives (e.g. 1,4-dioxane (DIOX), MORPH, cHANE). Both topologies comprise zero-dimensional (0D) pores (cavities) well suited by shape for cyclic small molecules such as those yielding them in the LAG screening. As mentioned before, when using cHANE as the liquid additive, we obtain both the **cag** and **neb** forms depending on the reaction conditions, with cHANE@**cag-ZnIm₂** being favored in Teflon™ jars and with shorter milling times. Based on literature precedent,⁵⁶ this implies that cHANE@**cag-ZnIm₂** is less thermodynamically stable than cHANE@**neb1-ZnIm₂**, and thus transforms into it upon prolonged milling.

Of the liquid additives studied, the **neb2-ZnIm₂** form is yielded exclusively by PYR which is also the solvent that was used for its original solvothermal synthesis (in a mixture with ethanol).⁸⁸ This suggests a templating effect that is transferable from solution to the solid state, but also might indicate a particularly strong stabilization of this framework form when PYR is encapsulated. Conversely, the **neb1-ZnIm₂** form is found using more different liquid additives, including thiophene (TPH), *N*-methylpyrrolidine (NMP1), and the six-membered aliphatic liquids (cHANE, DIOX and cyclohexene (cHENE)), including MORPH – the solvent used (in a mixture with ethanol) for the original solvothermal preparation of MORPH@**neb1-ZnIm₂**.⁸⁶ As mentioned, the **neb** cage building block of **neb1** is larger than that in **neb2**, which could explain the greater flexibility with regard to guest encapsulation, as it can potentially fit more sterically demanding guests than **neb2**. On the other hand, the **neb** cage in **neb2** is narrower (maximum pore diameter, = 4.05 Å, Figure 6, Table S9) than in **neb1** (= 4.97 Å), possibly explaining the need for planar aromatic pyridine. Interestingly, other than the mentioned polar cyclic molecules, **cag-ZnIm₂** is additionally templated by *N,N*-dimethylformamide (DMF), the solvent used (in a mixture with propylamine) for its original solvothermal synthesis.⁴⁷ and chloroform (CHCl₃). Both the **neb** and **cag** topologies thus demonstrate not only the possibility of transferring knowledge gained from solvothermal syntheses into mechanochemical synthesis, but also showcase the much broader toolbox of presumptive templates at hand when employing mechanochemistry, where reagent solubility and/or liquid miscibility are not an issue.

The **neb-ZnIm₂** topology appears in two forms, the previously mentioned **neb1**, and **neb2**. These forms have the same metal-ligand-metal connectivity, but due to the flexibility of the ZnIm₂ framework (resulting from changes in the relative orientations of imidazolate ligands) they have different pore sizes and shapes (Figure 6), and thus different porosity properties. For example, the **neb** cage building block of **neb1** is larger than that in **neb2**, resulting in a higher void fraction (8.1% in **neb1**, vs 6.0% in **neb2**, Table S9), and higher calculated surface area (237 m²/g in **neb1**, vs 1 m²/g in **neb2**, Table S4).

Following the **neb** and **cag** topologies, the **crb** family of frameworks appears using 10 out of 45 liquid templates. So far, three forms of **crb-ZnIm₂** have been reported in the literature: ZIF-2 (1.5DMF@**crb1-ZnIm₂**, CSD code VEJYIT²⁷), ZIF-64 (0.55DMF@**crb2-ZnIm₂**, CSD code GITTEJ³⁵), and ZIF-1 (0.5DMA@**crb3-ZnIm₂**, CSD code VEJYEP,²⁷ DMA = *N,N*-dimethylacetamide). These frameworks were all prepared solvothermally from DMF under different conditions (see Table S2). Despite possessing the same Zn-Im-Zn connectivity and thus the same topology, these three **crb** forms have different space groups, unit cell parameters, predicted surface areas and pore sizes (Table 1), revealing the considerable flexibility of the **crb-ZnIm₂** framework. This flexibility is a direct result of the conformational flexibility of the metal-ligand-metal linkages, which allows for large differences in the shapes of the **crb**-cage building blocks for the different **crb** forms (Figure 3). This makes **crb1**-, **crb2**- and **crb3-ZnIm₂** essentially different materials for potential porosity applications purposes.

Table 1. Porosity parameters of different forms of crb-ZnIm₂. The predicted specific surface area (SSA, N₂ at 77K), maximum pore diameter (d_{max}^{pore}), pore limiting diameter (d_{lim}^{pore}) and void fraction were all calculated using the Pore Analyzer function in Mercury. V_{UC} designates the unit cell volume, and T/V designates the density of metal atoms per unit volume.

	CSD code	space group	V _{UC} , Å ³	V _{UC} per Zn, Å ³	T/V, nm ⁻³	SSA, m ² /g	d_{max}^{pore} , Å	d_{lim}^{pore} , Å	void fraction, %
crb1	VEJYIT	<i>Pbca</i>	5706.6	356.7	2.80	1495	6.01	5.04	23.4
crb2	GITTEJ	<i>P2₁/n</i>	4414.4	275.9	3.62	465	6.80	1.70	11.9
crb3	VEJYEP	<i>P2₁/n</i>	2195.9	274.5	3.64	428	6.12	1.87	11.0
crbA	this work	<i>P2₁/c</i>	4503.7	281.5	3.55	511	6.40	1.96	12.0
crbT	this work	<i>Pnnm</i>	2571.4	321.4	3.11	321	4.75	3.66	14.7

During our screening, pure samples of **crb3-ZnIm₂** were successfully prepared by addition of DMA, oxetane (OXT), *N*-methyl-2-piperidone (NMPd) and *N*-methyl-2-pyrrolidone (NMP). Interestingly, the crystal structure of **crb3-ZnIm₂** deposited in the CSD (VEJYEP) contains DMA, despite the nominal crystallization solvent being DMF, indicating a potential preference of the framework for this guest. The **crb1-ZnIm₂** and **crb2-ZnIm₂** materials were prepared in our screening only as components of mixtures, using PYR (mixture with **neb2-ZnIm₂**, SI 2.1.40.) and hexamethylphosphoramide (HMPA, mixture with **crb3-ZnIm₂**, SI 2.1.22.), respectively. Since **crb1-ZnIm₂** and **crb2-ZnIm₂** have solvothermally only been prepared as single crystals in high-throughput experiments, it is not surprising that mechanochemistry is also only partially successful in their synthesis, providing them solely in mixtures with other forms. These two phases are also the least dense **crb** phases published to date (Table 1; void fractions: **crb1** – 23.4%, **crb2** – 11.9%, **crb3** – 11.0%), and may in the future be prepared pure using larger guests, especially in the case of **crb1**.

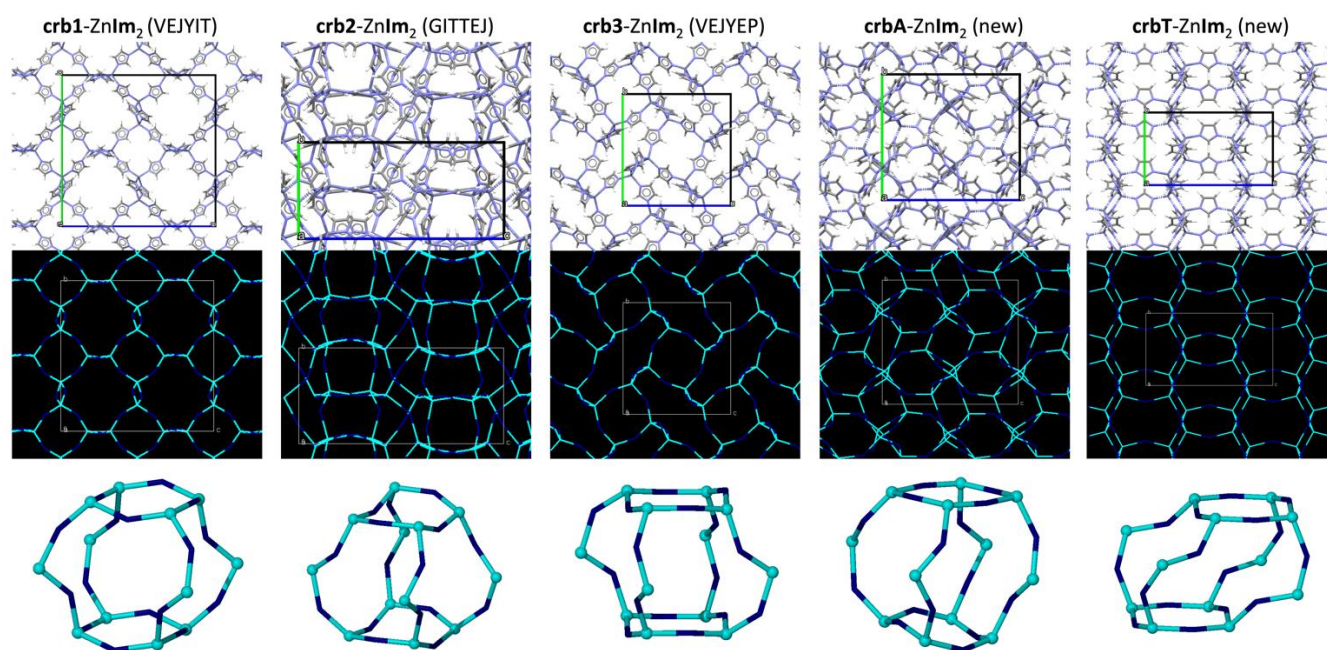


Figure 3. Graphical representations of the crb1, crb2, crb3, crbA and crbT forms of ZnIm₂. Top row: The crystal structures viewed along the *a* axis and presented through capped sticks representations. The unit cells are drawn in black, and any present guests have been removed from the structure. Middle row: The crystal packing represented in a reduced node-and-linker image, where zinc ions are depicted in light blue, whereas the centroids of imidazolate ions are depicted in dark blue. Bottom row: The crb building cages of each structure depicted through the reduced node-and-linker image.

2.4. New forms of *crb*-ZnIm₂. In further screening, mechanochemical reactions with added toluene (PhMe) and acetophenone (AcPhe) reproducibly gave phase-pure products whose PXRD patterns did not match any known ZIF forms. Attempts at solution-based syntheses of single crystals of these phases (SI-1.4.) were unsuccessful, potentially due to solubility constraints. We therefore resorted to crystal structure solution from PXRD data, assisted by periodic DFT calculations (see Materials and Methods, and SI-1.5., 1.6.). The new phases were found by Topos⁸⁹ and TopCryst⁹⁰ to both have the *crb* topology and were designated *crbT*-ZnIm₂ (from PhMe, Toluene) and *crbA*-ZnIm₂ (from AcPhe, Acetophenone). Their template content was found from Rietveld refinement (0.88 PhMe and 0.49 AcPhe, respectively) and by thermogravimetric analysis (TGA; 0.72 PhMe and 0.63 AcPhe, respectively). The average values of the two methods gave the final compositions of 0.8PhMe@*crbT*-ZnIm₂ and 0.56AcPhe@*crbA*-ZnIm₂. Both 0.8PhMe@*crbT*-ZnIm₂ and 0.56AcPhe@*crbA*-ZnIm₂ are crystallographically distinct from the three previously reported *crb* phases and have different calculated pore properties (Table 1). For example, *crbT* has the second highest calculated void fraction (14.7%) and per-zinc unit cell volume (321.4 Å³), while *crbA* has the second highest calculated maximum pore diameter (6.40 Å) of the known *crb* phases. Their physicochemical properties are also different; 0.56AcPhe@*crbA*-ZnIm₂ can be extensively washed with acetone and conserves its structure (Figure S3), while even short acetone washing of 0.8PhMe@*crbT*-ZnIm₂ results in a transformation into an unknown phase (Figure S38), presumably due to framework collapse upon guest exchange. Similarly, heating 0.8PhMe@*crbT*-ZnIm₂ results in the collapse into a mixture of the dense *coi*- and *zni*-ZnIm₂ phases (Figure S38). Interestingly, heating 0.56AcPhe@*crbA*-ZnIm₂ at 80 °C or 105 °C provides the *crb3* phase without observable loss of AcPhe guest, while heating at 150 °C results in the loss of absorbed AcPhe and the appearance of a novel phase characterized by low-angle peaks in the PXRD pattern, indicating a large unit cell and thus presumably a non-dense phase (Figure S3). While the *crbA* phase was found so far only through LAG with AcPhe, the *crbT* phase was also produced ed by anisole (PhOMe, Figure S39)) and 4-methylpyridine (4-MePyr, Figure S27) LAG reactions. It appears therefore that aromatic compounds with a single unbranched substituent favor the *crbT* phase, while a larger substituent on the aromatic core is needed to produce the *crbA* phase. This matches well with the larger maximum pore diameter in 0.56AcPhe@*crbA*-ZnIm₂ (6.40 Å, compared to 4.75 Å in 0.8PhMe@*crbT*-ZnIm₂), despite the larger void fraction in 0.8PhMe@*crbT*-ZnIm₂ (14.7 % compared to 12.0 % in *crbA*). With the addition of these new forms, the *crb* topology now has an unprecedented five crystallographically unique forms with different properties. Further research on the *crbA* and *crbT* phases is needed, but it is already evident that they have new and potentially interesting properties.

2.5. Preparation of low-density ZnIm₂ phases. Finally, the topologies that appeared least often in the LAG screening were also the least dense ones (theoretical activated densities between 0.85 and 1.15 g/cm³), namely *nog*-ZnIm₂ (from four out of 45 liquids, void fraction 15.8%) and *10mr*-ZnIm₂ (from one out 45 liquids, void fraction 20.5%). *nog*-ZnIm₂ immediately appeared without side products only using *N*-methylpiperidine (NMPP, Figure S34), but also appeared from the amorphous phase produced by milling with *N,N*-diethylformamide (DEF, Figure S11) after being aged for 12 days at ambient conditions. However, small peaks characteristic of unreacted ZnO (~32.1, 34.6 and 36.5 °2θ) were observed in the PXRD patterns of both product phases. This is likely due to the formation of a core-shell system where the ZnIm₂ grows on a ZnO core, as seen by Tanaka *et al.*⁶² In principle, it may be possible to convert the remaining ZnO to the ZIF product by additional milling, or by using nanoparticulate ZnO as a reagent.⁶² Since both procedures would add an additional parameter to our screening study, and potentially distort any structure-directing or pore-filling effects, we leave them for a follow-up study. Interestingly, *nog*-ZnIm₂ has large 1D channels going through the structures, so it is also possible that part of the imidazole reagent was absorbed into these channels and thus was unavailable for the reaction, lowering the yield. If so, using a larger amount of the pore-filling liquid, or an excess of imidazole might provide a higher yield.⁶⁹

The *10mr* phase was only found by LAG with DBF, the solvent from which it was originally prepared,⁴³ with larger amounts of solvent (either 167 or 200 μL, compared to the standard 100 μL) needed to avoid formation of the *moc*-Zn₄Im₃HIm side-product. Even then, in some repetitions of the synthesis, mixtures of products were obtained (Figure S10), potentially influenced by ambient conditions such as temperature, humidity, or other factors, so further work on this system is needed in the future. It is important to note that, while the original solvothermal reaction to produce *10mr*-ZnIm₂ required heating the reagents in DBF at 50 °C for 3 days, we were able to prepare 200 mg of form-pure product using only 167 μL of DBF in one hour of room-temperature milling. This demonstrates that our LAG screening is not only extremely successful at synthesizing different ZnIm₂ phases, but can also provide faster, cheaper, more efficient, and more environmentally friendly methods of MOF synthesis, once fully optimized.

2.6. Direct preparation of amorphous ZnIm₂. In addition to the presented crystalline phases, we also observed several cases of amorphous phases being directly synthesized by LAG. Specifically, 30 minutes of milling with *N*-methylcaprolactam (NMC, Figure S30) or *N*-methyl-2-piperidone (NMPd, Figure S32), as well as 60 min of milling with DEF (Figure S11) or NMPd gave amorphous products, presumably *a*-ZnIm₂, with small amounts of residual ZnO. The reaction with NMC was reproducible, and the amorphous phase remained stable for a minimum of seven days, but converted into unidentifiable crystalline phases after longer standing in ambient conditions. The amorphous phases resulting from the reactions with NMPd were stable for at least 20 days, while the amorphous products from DEF converted into the xDEF@**no**g-ZnIm₂ phase in less than 14 days of standing under ambient conditions. To the best of our knowledge, the only other direct synthesis of amorphous ZIFs (aZIFs) to date was done using 2-methylimidazole (**MeIm**), and involved encapsulation of the glucose oxidase enzyme from solution.⁹¹ All other syntheses of amorphous ZIFs involve first making a crystalline ZIF material, and then amorphizing it *via* heating, pressure or mechanochemistry.³⁸ As amorphous ZIFs have been the target of extensive studies and have potential applications,^{36–38,91–94} their direct and rapid synthesis is of potential interest in the future.

2.7. Periodic DFT calculations on empty frameworks. While LAG screening enabled a quick and efficient preparation of 13 different crystalline ZIFs as well as amorphous ZnIm₂ phases, and greatly expanded the scope of potential structure-directing agents in ZIF syntheses, the underpinnings of the presumptive templation effect remain unclear. We propose that the use of periodic DFT calculations will provide insight into the structure-directing process, and hopefully enable us to later conduct targeted LAG templation of specific desired MOF topologies. Periodic DFT has already been employed to elucidate the mechanochemistry of ZIFs, showing that polymorphic transformations of Zn(**MeIm**)₂ and Zn(**EtIm**)₂ (**EtIm** = 2-ethylimidazole) inside the mill follow the Ostwald rule of ripening, proceeding from the more open, thermodynamically less stable phases, toward the more stable, denser forms.⁵⁶ Furthermore, periodic DFT correctly surveyed the topological landscape of experimentally unknown ZIFs, in both a ligand-replacement experiment⁷⁶ and in the true crystal structure prediction of hypergolic ZIFs⁷⁷, allowing for their later mechanochemical synthesis. It has also been broadly used in assessing the relative stability of ZnIm₂ polymorphs,^{23,88,95–98} including generating hypothetical future ZIFs based on zeolite topologies.^{97–99} Some of these have then been synthesized, including the AFI and CAN topologies predicted in 2009⁹⁷ and synthesized in 2016⁴⁵, and the ATN topology predicted in 2009⁹⁷ and not synthesized until 2021.⁴⁴ All three topologies were prepared only by use of appropriate structure-directing agents (*N,N*-dipropylformamide (DPF) for AFI and CAN, and DBF with *N*-butylamine for the ATN phase), emphasizing their importance. Despite this, the vast majority of ZnIm₂ DFT modeling has only considered empty frameworks, discounting interactions with guests/presumptive templates. We therefore decided to pursue periodic DFT modeling of the frameworks obtained using LAG screening in their empty forms, and select guest-filled frameworks.

Several of the prepared ZnIm₂ frameworks had previously been modeled by periodic DFT calculations, namely the **cag**^{95,97,98} **crb1**⁹⁷ **crb3**⁹⁷ **neb2**⁹⁸ **coi**⁸⁸ and **zni**^{88,97,98} frameworks. It was shown that dispersion correction can have a crucial effect on the accuracy of energy rankings of ZIF polymorphs, and the Perdew, Burke and Ernzerhof (PBE) functional¹⁰⁰ combined with Grimme D2¹⁰¹ or D3¹⁰² semiempirical dispersion correction (PBE-D3) was found to best match the experimental crystallographic parameters.⁹⁵ D2 and D3 corrections appeared to perform similarly, though it was noted that the D2 correction tends to overbind.¹⁰² In ZIFs made from different ligands (such as **HMeIm** and **HEtIm**), PBE with Grimme D2 and, later, many-body dispersion (MBD*) correction also reproduced well the relative experimental energies of several ZIF topological forms.^{56,75–77} Furthermore, the performance of the PBE functional with TS, D3 and MBD* corrections was evaluated for the transformation of ZIF polymorphs to a ZIF carbonate phase upon exposure to carbon dioxide, and MBD* and D3 corrections showed best overall agreement with experimental energies determined from dissolution calorimetry.¹⁰³ We have ultimately decided to use the PBE-D3 method over PBE-MBD*, given their similar accuracy, but lower computational cost of the PBE-D3 method. All periodic DFT calculations were performed in the CASTEP¹⁰⁴ plane-wave DFT code.

We first performed geometry optimizations for the guest-free versions of all 13 zinc imidazolate frameworks obtained through LAG screening. The starting atom coordinates were obtained from the CSD, or *via* structure solution from PXRD data (**crbA** and **crbT** phases). All guests (if present) were removed from the frameworks, and disorder (if present) was resolved into components, all of which were separately optimized. Full details of all optimizations can be found in SI-1.6. and SI-2.5. The lowest energy structure was found to be the **moc-Zn₄(Im)₈HIm** material, which is also the product of the neat mechanochemical reaction between ZnO and **HIm**. Above it in energy are the topological polymorphs of ZnIm₂ and their different forms, whose energies are

reported relative to the **moc** phase (after accounting for the additional terminal imidazole molecule in **moc-Zn₄(Im)₈HIm**).

As previously reported^{95,97} the calculated energies of the optimized empty phases are roughly linearly proportional to their densities (Figure 4.a.). Thus, **moc-Zn₄(Im)₈HIm** is the global minimum, followed closely by **coi-ZnIm₂** ($\Delta E_{\text{moc}} = 2.66$ kJ/mol) and **zni-ZnIm₂** ($\Delta E_{\text{moc}} = 3.76$ kJ/mol). The very small calculated difference in energy for the **coi** and **zni** phases ($\Delta E_{\text{zni-coi}} = 1.10$ kJ/mol) likely explains the prevalence of their concomitant appearance in the LAG screening, and the reported ease of interconversion among them.^{23,88} The $\Delta E_{\text{zni-coi}}$ value also matches fairly well with the experimentally obtained value of the enthalpy of polymorphic transition between these two phases at 360 °C ($\Delta H_{\text{zni-coi}} = 2.9(1)$ kJ/mol).⁸⁸ Not surprisingly, these three most stable phases also appear most often in the LAG screening (Figure 4.b).

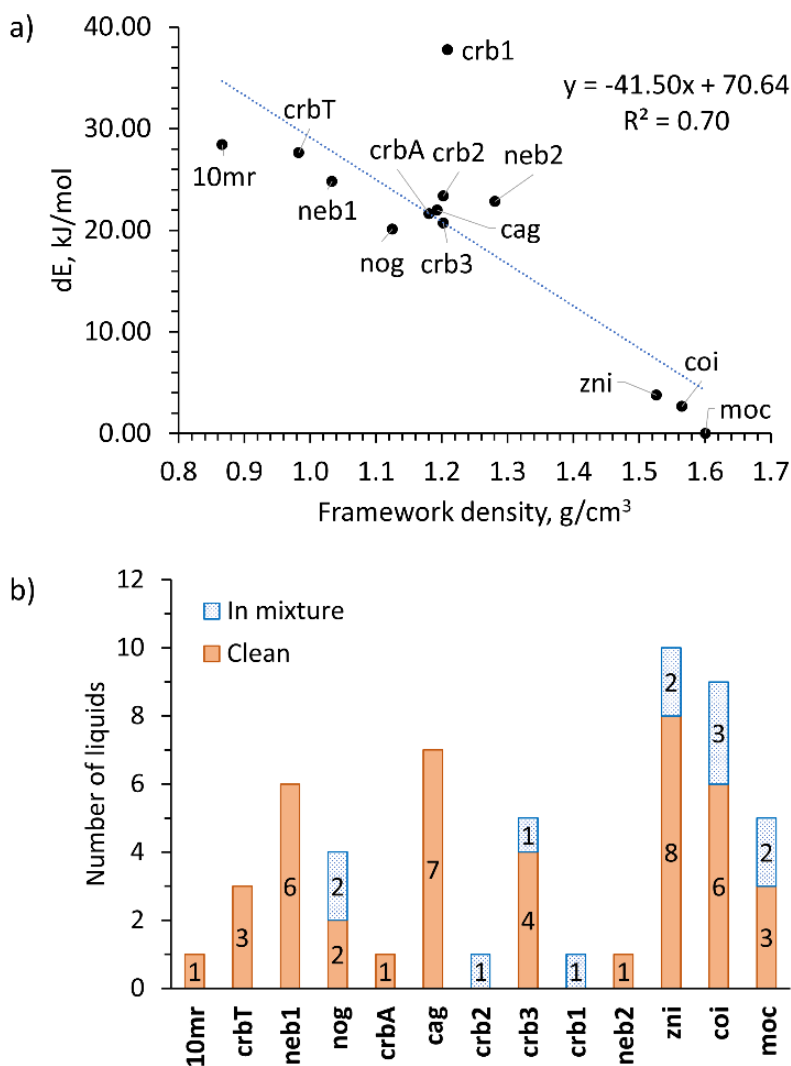


Figure 4. a) Comparison of the calculated energies of different topology empty ZnIm₂ frameworks and their densities. The reference point is the adjusted energy of **moc-Zn₄(Im)₈HIm₂**, and all energies are scaled per zinc atom. **b)** Number of liquids providing each topology in LAG screening, clean (orange bar) or as part of a mixture (blue bar). If a liquid provides the same topology both clean and in a mixture, it is only added to the “clean” number. The topological forms are listed in order of descending relative calculated energy.

A notable outlier from the observed energy vs. density trend is the **crb1** phase, which has the highest calculated relative energy ($\Delta E_{\text{moc}} = 37.77$ kJ/mol), while being the fifth most dense studied phase. It is therefore unsurprising that the **crb1** phase only shows up once in the LAG screening (with PYR), and only as part of a mixture (with the **neb2** phase). The newly found **crbT** form also has a high relative energy ($\Delta E_{\text{moc}} = 27.63$ kJ/mol), significantly larger than the **crbA** form ($\Delta E_{\text{moc}} = 21.61$ kJ/mol), which may explain why **crbT-ZnIm₂** collapses upon washing (guest exchange), while **crbA-ZnIm₂** easily maintains its form and crystallinity when

washed with acetone. On the other hand, **crbA-ZnIm₂** is very close in energy ($\Delta E_{\text{crbA-crB3}} = 0.90$ kJ/mol) to **crb3-ZnIm₂** ($\Delta_{\text{moc}} = 20.71$ kJ/mol), which may explain their aforementioned low-temperature (80°C) interconversion.

Other than **crb1-ZnIm₂**, the highest relative energy of the ZIFs found through mechanochemical screening belongs to the most porous phase, **10mr-ZnIm₂** ($\Delta E_{\text{moc}} = 28.42$ kJ/mol). That these frameworks can be experimentally observed during mechanochemical templation, even with an energy difference 20 or 25 kJ/mol above the most stable phases is quite extraordinary. It indicates a significant kinetic effect and/or a high degree of stabilization of the low density framework by the encapsulated guest. For reference, the observed energy difference between the highest and lowest energy forms in a mechanochemical reaction for ZIF frameworks based on other ligands is: 10.6 kJ/mol for **HMeIm**⁵⁶, 17.6 kJ/mol for **HEtIm**⁵⁶⁵⁶ and 15.6 kJ/mol for 2-trifluoromethylimidazole.⁷⁶ Moreover, the experimentally achievable ΔE_{moc} value can clearly be much higher, as we have previously achieved the mechanochemical synthesis of **RHO-ZnIm₂** (density = 0.74 g/cm³) by employing a designer, shape-persistent macrocyclic template.⁷⁹ Similarly, it has been shown that low density hydrogen bonded organic frameworks (HOFs) more than 50 kJ/mol in energy above the global minimum structure are experimentally accessible due to their stabilization by pore solvation.¹⁰⁵

2.8. Periodic DFT calculations on guest-occupied frameworks. We therefore decided to further explore the energetics of the LAG reactions by selecting several of the prepared frameworks and inserting additive molecules into their pores and cavities. Guest-filled structures were found or adapted from the CSD, in-house single crystal X-ray diffraction data, or solved PXRD crystal structures (see SI-2.5.3.). Then, the $x\text{guest}@y\text{ZnIm}_2$ composites were geometry optimized and their energies ($E(x\text{guest}@y\text{ZnIm}_2)$) were determined, taking into account the guest:framework stoichiometric ratio (*N.B.* these are non-dynamic 0K calculations). Separately, the guest molecules were geometry optimized in a large ($L_x = L_y = L_z = 25$ Å) box simulating the gas phase, and their energies ($E(\text{guest})$) were obtained. Full details can be found in SI-1.6 and SI-2.5. Subtracting the energies of the guest molecules (adjusted for stoichiometry) provides the energies of the **ZnIm₂** framework when it's occupied by guest ($E_{\text{occup}}(\text{ZnIm}_2)$), according to equation 1.

$$E_{\text{occup}}(\text{ZnIm}_2) = [E(x\text{guest}@y\text{ZnIm}_2) - xE(\text{guest})]/y \quad (1)$$

Comparison with the energies of the empty **ZnIm₂** frameworks (E_{empty}) provides the stabilization energy ΔE_{gas} that can be attributed to the guest being absorbed from the gas-phase (Equation 2).

$$\Delta E_{\text{gas}} = E_{\text{occup}} - E_{\text{empty}} \quad (2)$$

To account for the fact that our liquid additives are not in the gas phase, the obtained energies were adjusted for experimental enthalpies of evaporation according to equation 3, providing the stabilization energy ΔE_{liquid} that can be attributed to the guest being absorbed from the liquid phase:

$$\Delta E_{\text{liquid}} = \Delta E_{\text{gas}} + x/y E_{\text{vap}}(\text{guest}) \quad (3)$$

Arguably, the true stabilization energies are somewhere between ΔE_{gas} and ΔE_{liquid} , as many of the used liquids are volatile, and would be partially in the gas phase, especially under the highly dynamic milling conditions. In this case, we believe ΔE_{liquid} to be more representative of the experimental reality, and will refer to those values throughout the discussion. The dependence of the calculated energies for the empty frameworks of topologies found in our LAG screen, as well as the selected guest-occupied frameworks on their density are shown in Figure 5.

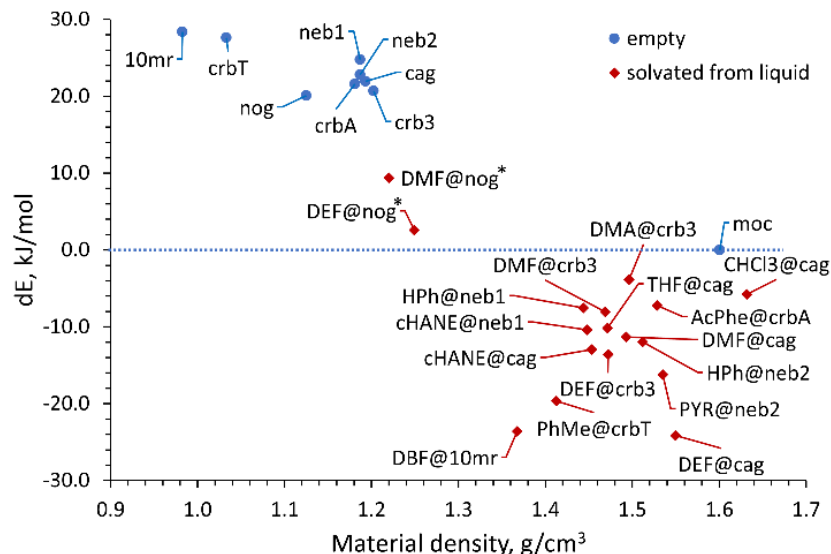


Figure 5. Dependence of the calculated relative energy for different topology empty ZnIm_2 frameworks (E_{empty} , blue circles) and guest-occupied ZnIm_2 frameworks (E_{occup} , red rhombuses) on their density. The reference point is the adjusted energy of **moc** topology framework (blue dotted line), and all enthalpies are scaled per zinc atom. The two **nog** topologies are marked with an asterisk due to potential issues with the starting structure.

The first observation is that almost all of the guest-occupied ZnIm_2 frameworks calculated have relative energies lower than the most stable empty framework, **moc**- $\text{Zn}_4\text{Im}_8\text{HIm}$, the most stable empty framework. The only exceptions are the two calculated **nog** topology solvates, 0.2DMF@**nog**- ZnIm_2 (DMF@**nog**, $\Delta E_{\text{moc, DMF}} = 9.38$ kJ/mol) and 0.2DEF@**nog**- ZnIm_2 (DEF@**nog**, $\Delta E_{\text{moc, DEF}} = 2.59$ kJ/mol). In our screening, the x DMF@**nog**- ZnIm_2 phase has not yet been observed, while the x DEF@**nog**- ZnIm_2 phase appears, but only by slow transformation from one of the amorphous phases. The DEF@**nog** phase is significantly lower in energy than the corresponding DMF phase ($\Delta E_{\text{DMF-DEF}} = 6.79$ kJ/mol), and much closer to **moc**- $\text{Zn}_4\text{Im}_8\text{HIm}$, so it is unsurprising that of the two, the DEF@**nog** phase is the only one experimentally observed. Even though both **nog** phases are significantly stabilized compared to the empty framework (by 17.47 and 10.68 kJ/mol for DEF and DMF, respectively), visual inspection of the optimized structures indicates that a significant volume of unoccupied space is still present (10.5% solvent accessible void space, or 613.6 Å³ per unit cell). It is possible that the single crystal providing the original structure of 0.2DEF@**nog**- ZnIm_2 was only partially solvated, and that the maximum amount of DEF that can be absorbed into **nog**- ZnIm_2 is actually higher. If the leftover void space were filled with more DEF, the stabilization would no doubt be greater, and it is likely that the energy of the x DEF@**nog**- ZnIm_2 structure would also fall below that of the **moc** phase global minimum. In the future we aim to obtain the fully occupied DEF@**nog** structure and, more generally, investigate the dynamical effects of the absorption of small-molecule guests into ZIF voids, therefore diminishing our reliance on published crystal structures.

In all the other optimized solvated forms of ZnIm_2 , the energy stabilization effects of the templates are even more pronounced. For **10mr**- ZnIm_2 , the stabilization upon inclusion of DBF, compared to the empty framework, is a staggering 51.96 kJ/mol, bringing the 0.4DBF@**10mr**- ZnIm_2 (DBF@**10mr**) material to 23.58 kJ/mol below **moc**- $\text{Zn}_4\text{Im}_8\text{HIm}$. Looking at the geometry optimized crystal structure of DBF@**10mr**, not only is the formerly empty space within the framework now completely filled (void fraction 0.1%), but the DBF molecules are connected to the framework imidazolates by a series of (imidazolate) C-H \cdots O (amide) hydrogen bonds (Figure S75). This abundance of intermolecular van der Waals interactions and C-H \cdots O hydrogen bonds not only stabilizes the framework, but also potentially indicates a true templation effect of DBF molecules in the synthesis of DBF@**10mr**. Namely, the directionality of the C-H \cdots O hydrogen bonds could serve as a way to pre-organize imidazol(at)e molecules around the DBF structure-directing molecules in the early stages of the reaction, so that the **10mr** topology is highly favored as a product.

A similar degree of stabilization is achieved for the **crbT** phase when it is occupied by toluene. The 0.8PhMe@**crbT**- ZnIm_2 (PhMe@**crbT**) phase is 47.24 kJ/mol lower in energy than the empty **crbT**- ZnIm_2 phase, and 19.64 kJ/mol more stable than **moc**- $\text{Zn}_4\text{Im}_8\text{HIm}$. In this case, the stabilization is almost exclusively due to space-filling (void fraction is 0.0%) and van der Waals interactions, as toluene is unable to form hydrogen bonds

with the framework. In comparison, the stabilization of the **crbA** phase is significantly smaller. $0.56\text{AcPhe@crbA-ZnIm}_2$ (AcPhe@crbA) is 20.24 kJ/mol more stable than the empty framework, and only 7.22 kJ/mol more stable than **moc-Zn₄Im₈HIm**. However, this smaller guest-induced stabilization might also help explain why the **crbA** framework is stable upon guest exchange, whereas the **crbT** framework easily collapses without the exceptional stabilization provided by the toluene guest.

Looking at the **neb** topology ZnIm_2 materials, we see that $0.5\text{PYR@neb2-ZnIm}_2$ (PYR@neb2) is stabilized by inclusion of pyridine ($\Delta E = -39.03$ kJ/mol), putting it at 16.23 kJ/mol below **moc-Zn₄Im₈HIm**. The $0.5\text{cHANE@neb1-ZnIm}_2$ (cHANE@neb1) phase is slightly less effectively stabilized by cyclohexane ($\Delta E = -35.15$ kJ/mol), yet remains at 10.39 kJ/mol below **moc-Zn₄Im₈HIm**. Since both **neb** template@ ZnIm_2 phases are fully filled (solvent accessible void fraction is 0.0% for both), the extra stabilization in the **neb2** phase is likely attributable to weak C-H \cdots N interactions connecting the pyridine nitrogen to the framework imidazolates (Figure S76). Indeed, if the PYR guest in **neb2-ZnIm₂** is replaced by benzene (HPh) *in silico*, the stabilization is lowered by 4.28 kJ/mol ($\Delta E_{\text{empty}} = -34.75$ kJ/mol, $\Delta E_{\text{moc}} = -11.95$ kJ/mol), and is very close to the stabilization of **neb1-ZnIm₂** by the cHANE template. These C-H \cdots N interactions might serve as a pathway to true templation and ligand pre-organization, explaining why PYR is the only additive yielding the **neb2-ZnIm₂** phase. Conversely, if cHANE in **neb1** is also replaced by HPh, the degree of stabilization is lessened ($\Delta E_{\text{empty}} = -32.30$ kJ/mol, $\Delta E_{\text{moc}} = -7.53$ kJ/mol), demonstrating the importance of molecular shape for the stabilization of **neb1-ZnIm₂**. Namely, bulkier, non-planar aliphatic 6-membered rings in the chair conformation fit the wider **neb1** cage much better than flat aromatic rings (Figure 6).

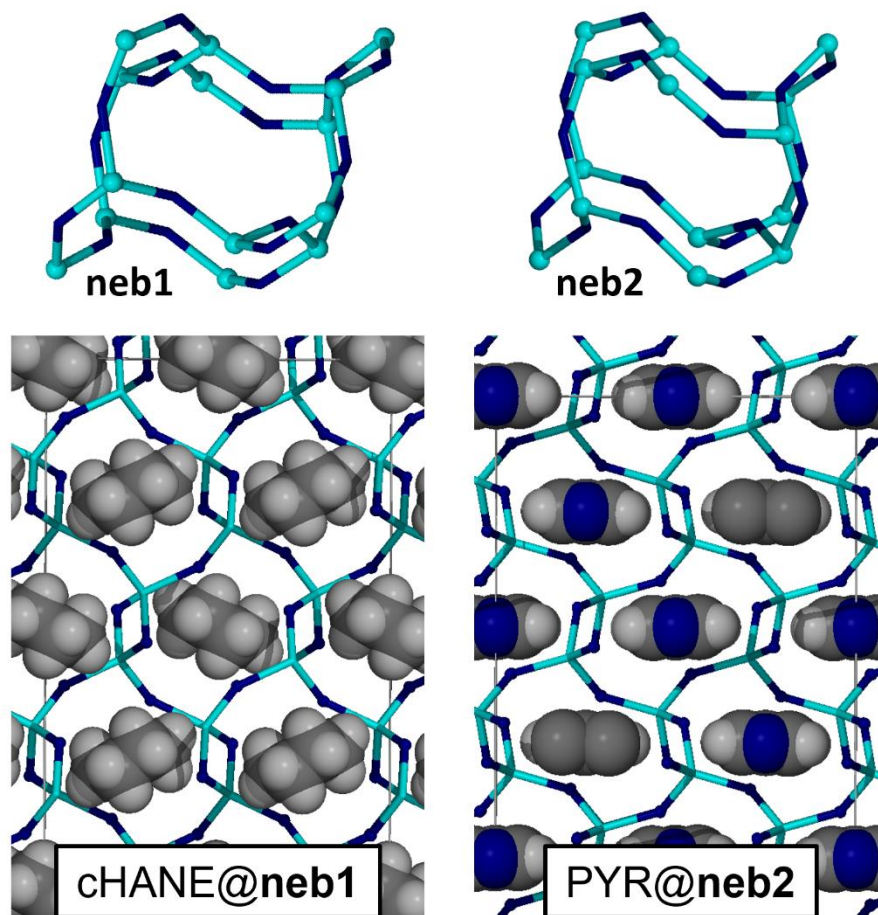


Figure 6. Comparison of the crystal structures of the DFT-optimized **cHANE@neb1** and **PYR@neb2** phases, and their **neb** cages. The frameworks and cages are shown in the node-and-linker representations (light blue = Zn, dark blue = Im- centroid), while the template molecules are shown in spacefill and CPK colour.

For **cag-ZnIm₂**, we tested five different template molecules, chloroform (CHCl_3), DMF, DEF, tetrahydrofuran (THF) and cHANE. All five additives provide solvated $0.5\text{guest@cag-ZnIm}_2$ (guest@cag) phases calculated to be more thermodynamically stable than **moc-Zn₄Im₈HIm**, with relative energies in the following order: DEF@cag , -24.13 kJ/mol < cHANE@cag , -12.94 kJ/mol) < DMF@cag , -11.33 kJ/mol < THF@cag , -10.17

kJ/mol) < CHCl₃@**cag**, -5.76 kJ/mol. Unexpectedly, the most stable of the guest@**cag**-ZnIm₂ phases according to our calculations – DEF@**cag** – is the only one we do not observe experimentally. The DEF additive instead provides the aforementioned amorphous phase that transforms into the DEF@**nog** phase, which is significantly less stable by our calculations than the DEF@**cag** phase ($\Delta E_{\text{cag-nog}} = 26.72$ kJ/mol). However, insertion of more DEF molecules into the DEF@**nog** phase may drastically change the relative thermodynamics of these phases, and shed more light on the current discrepancies between calculation and experiment.

Another interesting case is that of the cHANE@**cag** phase. As previously mentioned, shorter milling results in the cHANE@**cag** phase, while longer milling provides the cHANE@**neb1** phase (Figure 7a). Ostwald's rule of stages, which is considered generally applicable in mechanochemistry,^{56,71} would imply that cHANE@**cag** should be the thermodynamically less stable phase. Our calculations, however, suggest the opposite: cHANE@**cag** is calculated to be more stable than cHANE@**neb1** by $\Delta E_{\text{cag-neb}} = 2.55$ kJ/mol; a small but non-negligible amount. Comparison of the optimized crystal structures shows that cHANE@**neb1** is densely packed, but cHANE@**cag** still has a small amount of accessible space (4.1% void space), enough to ensure some mobility of the cHANE molecules in an otherwise inaccessible 0D cavity (Figure 7b). We hypothesize that in the highly dynamic ball milling environment, where particles are constantly being comminuted and new surfaces are opening, cHANE molecules have the opportunity to escape cHANE@**cag** and nucleate cHANE@**neb1**. cHANE molecules appear to then be kinetically locked inside cHANE@**neb1**, and the material is stabilized enough to withstand further milling. Kinetic and entropic effects such as these are impossible to assess *via* periodic DFT calculations, again emphasizing the need for dynamic modeling.

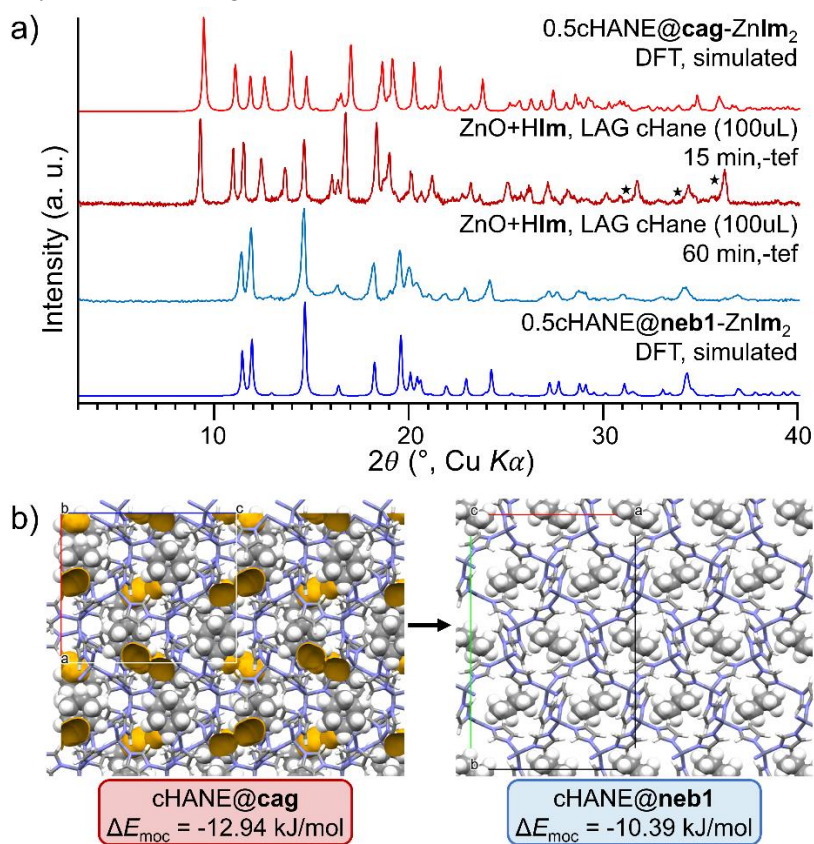


Figure 7. a) Comparison of experimental PXRD patterns of products of milling ZnO and HIm with cyclohexane (cHANE) for 15 and 60 minutes with simulated PXRD patterns of the DFT-optimized cHANE@**cag** and cHANE@**neb1** phases. Black stars denote peaks of leftover ZnO reagent. b) Comparison of the crystal structures of the DFT-optimized cHANE@**cag** and cHANE@**neb1** phases, and their relative energies compared to moc-Zn₄Im₈HIm. Voids in the crystal structures are shown in yellow contour.

Similar to cHANE@**cag**, the structure of THF@**cag** contains some voids (1.8% void space), which is reflected in the experimental behavior. Namely, despite the stabilization of THF@**cag** compared to the empty framework ($\Delta E_{\text{empty}} = -32.12$ kJ/mol), longer milling times or longer standing in ambient conditions facilitate the framework's collapse into the denser **coi**-ZnIm₂ phase (Figure S44). Presumably, the voids facilitate the escape of THF molecules from the framework, allowing it to collapse into **coi**-ZnIm₂. Conversely, CHCl₃@**cag** survives 60

min of milling, and appears to be the sole thermodynamic product of mechanochemical synthesis, despite the voids in its structure (1.5%). This result could potentially be attributed to a slightly higher vapor pressure of THF compared to CHCl_3 , but could also be due to other factors, such as particle size, surface energy, etc. For example, it is well known that stability of different polymorphs can vary widely depending on their particle size¹⁰⁶ which in turn varies depending on the liquid additive or milling conditions.

The third most stable **cag**- ZnIm_2 solvate modeled is 0.5DMF@cag-ZnIm_2 (DMF@cag , $\Delta E_{\text{moc-cag}} = -11.33$ kJ/mol). Other than DMF@cag , we optimized DMF as the guest in two other frameworks, namely 0.2DMF@nog-ZnIm_2 (DMF@nog) and $0.5\text{DMF@crb3-ZnIm}_2$ (DMF@crb3). Of the three solvates, DMF@cag has the lowest energy ($\Delta E_{\text{moc-nog}} = +9.38$ kJ/mol for DMF@nog and $\Delta E_{\text{moc-crb3}} = -8.05$ kJ/mol for DMF@crb3), and it is the phase experimentally obtained during LAG screening (Figure 8). This agreement between the calculations and experiment strengthens our confidence in the chosen computational method.

Other than DMF@crb3 , we modeled other guest@**crb3** phases, namely $0.5\text{DMA@crb3-ZnIm}_2$ (DMA@crb3) and $0.5\text{DEF@crb3-ZnIm}_2$ (DEF@crb3). The lowest in energy appeared to be the DEF@crb3 phase ($\Delta E_{\text{DEF}} = -13.60$ kJ/mol). However, the DEF@cag phase was even lower in energy, and as mentioned before, it is difficult to predict what the energy of the DEF@nog phase would be when fully occupied. Logically, DEF ought not yield **crb3**- ZnIm_2 , when at least one lower energy phase is available as product. The next lowest in energy would be the DMF@crb3 phase, but again, there exists a lower energy phase encapsulating DMF, DMF@cag . The remaining guest@**crb3** phase, DMA@crb3 , while highest in energy of the three **crb3** phases we calculated, still achieves significant stabilization compared to the empty **crb3**- ZnIm_2 ($\Delta E_{\text{empty}} = -24.54$ kJ/mol) and falls below **moc**- $\text{Zn}_4\text{Im}_8\text{HIm}$ ($\Delta E_{\text{moc}} = -3.86$ kJ/mol). It is therefore unsurprising that the addition of DMA in LAG screening results in the **crb3** phase (Figure 8).

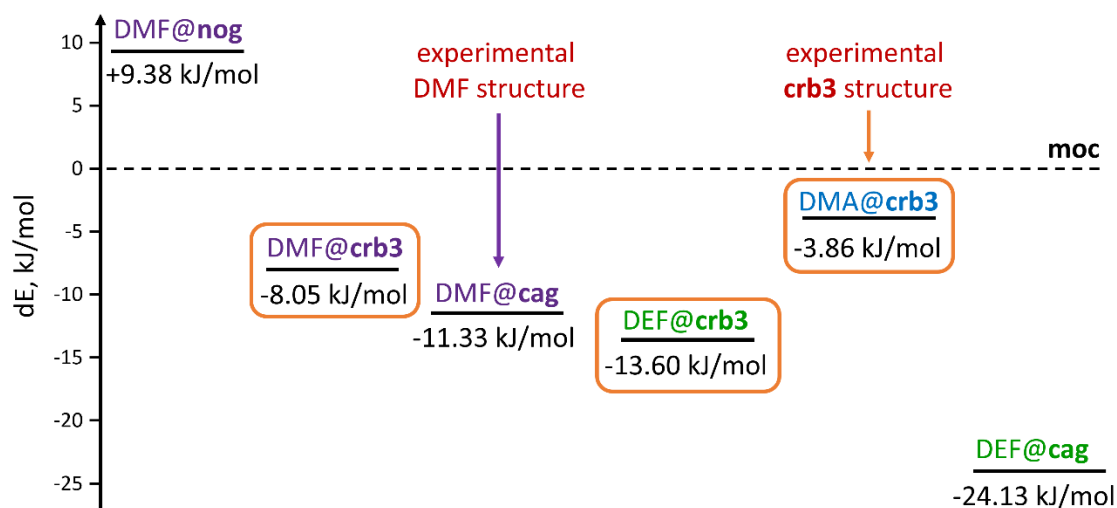


Figure 8. Comparison of energies for different DMF, DEF and **crb3** phases. Materials containing DMF, DEF and DMA are marked in purple, green and blue, respectively, while the three **crb3** phases are circled in orange.

3. Conclusions

Overall, we have demonstrated a novel, fast, highly effective method to screen for ZIF topologies by using small liquid additives as structure-directing agents in mechanochemical synthesis. We tested 45 different potential additives and prepared 7 different ZnIm_2 topologies in 12 different crystalline forms, including two new forms of **crb3**- ZnIm_2 , as well as the **moc**- $\text{Zn}_4\text{Im}_8\text{HIm}$ material and amorphous phases. We showed that strategies and putative templates used in solvothermal ZIF syntheses can be loosely translated to our mechanochemical screening, but that our scope of structure-directing agents is significantly broadened since reagent solubility is not a constraint.

Periodic DFT calculations performed on guest-free and solvated structures of the obtained zinc imidazolate solid forms strongly suggest that these systems are ultimately governed by thermodynamics, with structure stabilization achieved by effective pore solvation. In addition, we have shown that by comparing the energetics of different frameworks containing the same additive, we can predict which of them will be experimentally favored. This work illustrates the potential predictive power of combining periodic DFT calculations with mechanochemical screening for MOF syntheses. In the future, it ought to be possible to conduct additive screenings *in silico*, saving precious experimental resources. However, the success of DFT modeling depends on

the starting model used, so combining DFT with dynamical methods to obtain better starting models and probe the effects of different structure-directing agents might offer many benefits for the future. In addition, we are currently unable to model the kinetics of these syntheses, which is sorely needed to successfully make predictions about the outcomes of mechanochemical templation of ZIFs. However, we believe this work presents great strides towards that end goal.

4. Materials and methods

Full details of all methods and experimental procedures can be found in the Supplementary Information (SI). All chemicals were purchased (SI-1.1) and used without further purification.

Powder X-ray diffraction (PXRD) patterns were collected using either a Bruker APEX II DUO CCD area-detector diffractometer operating in transmission mode (DUO), a Bruker D2 powder X-ray diffractometer in Bragg-Brentano mode (D2), or a Panalytical Aeris powder X-ray diffractometer in Bragg-Brentano mode (Aeris). The PXRD patterns were collected in the $3\text{--}45^\circ$ 2θ range using Cu-K α radiation ($\lambda=1.5418$ Å), with the sample mounted on a silicon (Aeris) or plastic plate (D2), or in a Kapton capillary (DUO). Capillary PXRD data for structure solution were collected at room temperature (RT) on a Malvern Panalytical Empyrean diffractometer using Cu-K α radiation ($\lambda=1.5418$ Å), collecting from 2 to $70^\circ 2\theta$ with a step size of 0.0077° and 80 s exposure time with the sample mounted in a Kapton capillary. High resolution synchrotron PXRD data for structure solution were collected using beamline 11-BM at the Advanced Photon Source (APS), Argonne National Laboratory using an average wavelength of 0.412602 Å, with the sample mounted in a Kapton capillary.

Single crystals of the CHCl₃, THF and DEF solvates of cag-ZnIm₂ were all prepared by soaking single crystals of $0.5\text{DMF}@cag\text{-ZnIm}_2$ (synthesized according to Park *et al*²⁷) in the corresponding solvent over several weeks, with periodic exchanges of the soaking solvent.

Single crystal X-ray diffraction (SCXRD) data were collected on a Bruker-AXS APEX II DUO single crystal diffractometer equipped with an Oxford Cryosystems 700 Cryostream, using Mo K α radiation (0.71073 Å). The crystal structures were solved by direct methods using SHELXS¹⁰⁷ and all structural refinements were conducted using SHELXL-2014-7¹⁰⁸. All hydrogen atoms were placed in calculated positions and were refined using a riding model with coordinates and isotropic displacement parameters depending upon the atom to which they are attached.

Thermogravimetric analyses (TGA) were conducted on a Simultaneous Thermal Analyzer (STA) 6000 (PerkinElmer, Inc.) in alumina crucibles at heated at a rate of 7 or $10^\circ\text{C}/\text{min}$ from 35°C to 500 or 700°C under dynamic atmosphere of nitrogen or oxygen gas with a flow rate of 20 mL/min.

Milling reactions were conducted in a 14 mL TeflonTM (Form-Tech Scientific or InSolido Technologies) or stainless steel (InSolido Technologies) jar with one 7 mm (1.4 g) and one 9 mm (3.5 g) stainless steel ball bearing. In a typical liquid assisted grinding (LAG) reaction, 100 μL (or 200 μL or an equimolar amount compared to zinc, if so noted) of a given liquid was added into a milling jar containing the ball bearings, zinc oxide (75.0 mg, 0.92 mmol) and imidazole (125.5 mg, 1.84 mmol). The samples were milled at 30 Hz for $15\text{--}90$ min using a Retsch MM400 ball mill or an InSolido Technologies IST-500 mixer mill. The products were collected by scraping with a spatula and analyzed without washing or further purification. To avoid cross-contamination, the milling balls and jars were cleaned by milling a mixture of sodium hydrogencarbonate and laboratory solid detergent (Sparkleen or Vim) with a few drops of added ethanol or water for 15 min at 30 Hz frequency after every use, and then washed with soap and water, and rinsed with DI water and ethanol.

Structure solution from PXRD data. The PXRD patterns of $0.8\text{PhMe}@c\text{rbT-ZnIm}_2$ and $0.56\text{AcPhe}@c\text{rbA-ZnIm}_2$ were indexed using DICVOL06¹⁰⁹ and NTREOR¹¹⁰ algorithms, as implemented in the program EXPO2014¹¹¹ followed by Le Bail pattern decomposition¹¹² and space group determination. Direct methods structure solution was then performed in the same program, determining the positions of Zn centers. The imidazolate ligand positions were either found from electron density (for $0.8\text{PhMe}@c\text{rbT-ZnIm}_2$) or inserted manually (for $0.56\text{AcPhe}@c\text{rbA-ZnIm}_2$). Pawley refinement, simulated annealing structure solution and Rietveld refinement were performed using TOPAS v7¹¹³. Peaks of ZnO impurity (in the **crbT** structure, COD code 1011258¹¹⁴) were explicitly modeled in all procedures, using the known ZnO structure and unit cell parameters. Positions of guest molecules (toluene and acetophenone) were found through the Simulated Annealing (SA) algorithm, where only the positions, orientations and occupancies of guest molecule fragments were allowed to vary. Both structures were then subjected to Rietveld refinement. Cycles of periodic DFT optimization (with unit cell parameters fixed to their experimental values) and subsequent Rietveld refinement using DFT-optimized rigid

bodies were then performed for both materials until a satisfactory final structure was achieved. Full details of the employed procedures can be found in sections SI-1.5, SI-1.6 and SI-2.3.2.

A preliminary structure for 0.5cHANE@**neb1-ZnIm**₂ was prepared from the isostructural cyclohexanol solvate of Co**Im**₂ (CSD code EQOCES²⁹). Rietveld refinement for 0.5cHANE@**neb1-ZnIm**₂ was then performed using TOPAS v7¹¹³ refining the position of the Zn atom, while positions and orientations of imidazolate and cyclohexane fragments were refined with rigid body constraints. Peaks of ZnO (COD code 1011258¹¹⁴) and **moc-Zn₄Im₈(HIm)** (CSD code KUMXEW³⁹) impurities were explicitly modeled and a mixed-phase refinement performed. The resulting structural model was then subjected to periodic DFT geometry optimization with unit cell parameters fixed at their experimental values. The DFT-optimized structure was then used to define the rigid body for the final refinement cycle. Full details of the employed procedures can be found in sections SI-1.5, SI-1.6 and SI-2.3.1.

Periodic DFT calculations were performed with the plane-wave DFT code CASTEP 19.1 or 20.1.¹⁰⁴ The input files were prepared from crystal structures solved from SCXRD and PXRD data, or obtained from the CSD. In each crystal structure disorder was resolved into components which were individually optimized and the lowest energy structure was taken into consideration. Prior to geometry optimization, C-H bond lengths were normalized to a value of 1.088 Å in Mercury, in order to speed up the optimization towards the energy minimum geometry.

For the empty ZIF structures, all guests were deleted from the parent framework, and for the guest-filled structures, guests were either taken directly from a solved or published crystal structure, or a preliminary guest structure was generated inside the framework pores using X-Seed¹¹⁵ (see SI-2.5.3). CASTEP-compatible .cell files were then generated for empty ZIFs, gas-phase guests and the ZIF-guest complexes using the cif2cell¹¹⁶ program. All structures with I-, C- or F-centered lattices were transformed to the corresponding primitive structure with the aim of reducing the cell volume and, thus, the computational cost of the DFT calculation. This transformation preserved all the symmetry operations of the original structure. An optimization of DFT parameters was performed using **moc-Zn₄Im₈(HIm)** (CSD code KUMXEW) as the model structure (section SI-2.5.1). The plane wave basis set was truncated at 800 eV cutoff and ultrasoft on-the-fly generated pseudopotentials were used to attenuate Coulomb potential in the core regions. Electronic calculations were performed with PBE functional¹⁰⁰ combined with Grimme D3¹⁰² semiempirical dispersion correction. The electronic Brillouin zone was sampled with a 0.06 Å⁻¹ k-point spacing. Crystal structures were optimized with respect to unit cell parameters and atom positions, subject to space group symmetry constraints. The geometry convergence criteria were set as follows: maximum energy change: 1x10⁻¹⁰ eV atom⁻¹; maximum atom displacement: 0.001 Å; maximum atomic force: 0.05 eV Å⁻¹; maximum value of stress tensor parameters: 0.05 GPa. Example input files can be seen in the SI-2.5.2.

Gas-phase energies of guest molecules were also calculated, by placing each guest molecule in a large cubic cell ($L_x = L_y = L_z = 25$ Å) and optimizing the geometry. The unit cell dimensions were kept fixed to prevent contraction of the simulation box and aggregation of the molecules located in the periodic images of the simulation cell. The electronic Brillouin zone was sampled with the Γ k-point, and all the other calculation parameters were set the same as for the geometry optimization of the ZIF crystal structures.

ASSOCIATED CONTENT

Supporting Information.

Details of synthetic procedures, periodic DFT calculations, crystal structure solution and characterization methods; PXRD analyses of all reactions; TGA data for **crbT** and **crbA** materials; graphs and tables summarizing the computational results, including optimizations of parameters; example input files used for calculations; images of crystal structures; tables summarizing the templates used, the reaction outcomes, and materials properties (PDF)

Accession Codes

CCDC codes 2381139-2381143 and 2423969 contain the supplementary crystallographic data for this paper. These data can be obtained free of charge via www.ccdc.cam.ac.uk/data_request/cif, or by emailing data_request@ccdc.cam.ac.uk, or by contacting The Cambridge Crystallographic Data Centre, 12 Union Road, Cambridge CB2 1EZ, UK; fax: +44 1223 336033.

AUTHOR INFORMATION

Corresponding Authors

*Ivana Brekalo, Division of Physical Chemistry, Ruđer Bošković Institute, Zagreb, Croatia; Email: ibrekalo@irb.hr

*Mihails Arhangel'skis, Faculty of Chemistry, University of Warsaw, Warsaw, Poland; Email: m.arhangel'skis@uw.edu.pl

*Tomislav Frišćić, School of Chemistry, University of Birmingham, Birmingham, UK; Email: t.fris'cic@bham.ac.uk

*K. Travis Holman, Department of Chemistry, Georgetown University, Washington, D.C., USA; Email: kth7@georgetown.edu

Author Contributions

The manuscript was written through contributions of all authors. All authors have given approval to the final version of the manuscript.

Funding Sources

This work has been supported by the “Developing Research Support” Program of the Croatian Ministry of Science and the Croatian Science Foundation, funded by the European Union from the NextGenerationEU programme through grant NPOO.C3.2.R2-I1.06.0049. I.B. acknowledges support from the Polish National Agency for Academic Exchange (Ulam Scholarship PPN/ULM/2020/1/00216). M.A. acknowledges the support of National Science Centre of Poland (NCN) for the support via grants 2018/31/D/ST5/03619 and 2023/51/B/ST5/01555. Y.X. thanks NCN for the PhD scholarship funded by the grant 2018/31/D/ST5/03619.

We are grateful for computational support from the Croatian High Performance Computing Competency Center (HR HPC CC), the UK national high performance computing service, ARCHER2, for which access was obtained via the UKCP consortium and funded by EPSRC grant ref EP/X035891/1, the PLGrid Consortium (grant PLG/2023/016775), and the Digital Research Alliance of Canada for access to supercomputer Cedar.

This research used resources of the Advanced Photon Source, a U.S. Department of Energy (DOE) Office of Science User Facility operated for the DOE Office of Science by Argonne National Laboratory under Contract No. DE-AC02-06CH11357. The mail-in program at Beamline 11-ID-B (and/or 17-BM, 11-BM) contributed to the data under the rapid access proposal 41701.

ACKNOWLEDGMENT

The authors would like to thank Drs Krunoslav Užarević, Nikola Cindro and Anamarija Knežević for help with acquiring some of the chemicals. IB would like to thank Dr Krunoslav Užarević for support and helpful discussions. We would like to thank Dr Saul Lapidus for help with the acquisition of high resolution PXRD data.

REFERENCES

- (1) Gardner, C. R.; Walsh, C. T.; Almarsson, Ö. Drugs as Materials: Valuing Physical Form in Drug Discovery. *Nat Rev Drug Discov* **2004**, *3* (11), 926–934. <https://doi.org/10.1038/nrd1550>.
- (2) Couillaud, B. M.; Espeau, P.; Mignet, N.; Corvis, Y. State of the Art of Pharmaceutical Solid Forms: From Crystal Property Issues to Nanocrystals Formulation. *ChemMedChem* **2019**, *14* (1), 8–23. <https://doi.org/10.1002/cmdc.201800612>.
- (3) Aaltonen, J.; Alleso, M.; Mirza, S.; Koradia, V.; Gordon, K.; Rantanen, J. Solid Form Screening – A Review. *European Journal of Pharmaceutics and Biopharmaceutics* **2009**, *71* (1), 23–37. <https://doi.org/10.1016/j.ejpb.2008.07.014>.
- (4) Chemburkar, S. R.; Bauer, J.; Deming, K.; Spiwek, H.; Patel, K.; Morris, J.; Henry, R.; Spanton, S.; Dziki, W.; Porter, W.; Quick, J.; Bauer, P.; Donaubaue, J.; Narayanan, B. A.; Soldani, M.; Riley, D.; McFarland, K. Dealing with the Impact of Ritonavir Polymorphs on the Late Stages of Bulk Drug Process Development. *Org Process Res Dev* **2000**, *4* (5), 413–417. <https://doi.org/10.1021/op000023y>.

- (5) Kirchon, A.; Feng, L.; Drake, H. F.; Joseph, E. A.; Zhou, H.-C. From Fundamentals to Applications: A Toolbox for Robust and Multifunctional MOF Materials. *Chem Soc Rev* **2018**, *47* (23), 8611–8638. <https://doi.org/10.1039/C8CS00688A>.
- (6) Zhao, D.; Zhao, T. Pore Engineering for High Performance Porous Materials. *ACS Cent Sci* **2023**, *9* (8), 1499–1503. <https://doi.org/10.1021/acscentsci.3c00916>.
- (7) Wang, A.; Ma, Y.; Zhao, D. Pore Engineering of Porous Materials: Effects and Applications. *ACS Nano* **2024**, *18* (34), 22829–22854. <https://doi.org/10.1021/acsnano.4c08708>.
- (8) Hua, M.; Ding, Y.; Lv, C.; Han, N.; Chu, K. Tailoring Functionalities: Pore Engineering Strategies in Porous Organic Cages for Diverse Applications. *J Mater Chem A Mater* **2025**, *13* (3), 1641–1658. <https://doi.org/10.1039/D4TA07124G>.
- (9) Eddaoudi, M.; Kim, J.; Rosi, N.; Vodak, D.; Wachter, J.; O’Keeffe, M.; Yaghi, O. M. Systematic Design of Pore Size and Functionality in Isorecticular MOFs and Their Application in Methane Storage. *Science (1979)* **2002**, *295* (5554), 469–472. <https://doi.org/10.1126/science.1067208>.
- (10) Dey, C.; Kundu, T.; Biswal, B. P.; Mallick, A.; Banerjee, R. Crystalline Metal–Organic Frameworks (MOFs): Synthesis, Structure and Function. *Acta Crystallogr B Struct Sci Cryst Eng Mater* **2014**, *70* (1), 3–10. <https://doi.org/10.1107/S2052520613029557>.
- (11) Farha, O. K.; Hupp, J. T. Rational Design, Synthesis, Purification, and Activation of Metal–Organic Framework Materials. *Acc Chem Res* **2010**, *43* (8), 1166–1175. <https://doi.org/10.1021/ar1000617>.
- (12) Eddaoudi, M.; Sava, D. F.; Eubank, J. F.; Adil, K.; Guillermin, V. Zeolite-like Metal–Organic Frameworks (ZMOFs): Design, Synthesis, and Properties. *Chem Soc Rev* **2015**, *44* (1), 228–249. <https://doi.org/10.1039/C4CS00230J>.
- (13) Yaghi, O. M.; O’Keeffe, M.; Ockwig, N. W.; Chae, H. K.; Eddaoudi, M.; Kim, J. Reticular Synthesis and the Design of New Materials. *Nature* **2003**, *423* (6941), 705–714. <https://doi.org/10.1038/nature01650>.
- (14) Hendon, C. H.; Rieth, A. J.; Korzyński, M. D.; Dincă, M. Grand Challenges and Future Opportunities for Metal–Organic Frameworks. *ACS Cent Sci* **2017**, *3* (6), 554–563. <https://doi.org/10.1021/acscentsci.7b00197>.
- (15) Freund, R.; Zaremba, O.; Arnauts, G.; Ameloot, R.; Skorupskii, G.; Dincă, M.; Bavykina, A.; Gascon, J.; Ejsmont, A.; Goscianska, J.; Kalmutzki, M.; Lächelt, U.; Ploetz, E.; Diercks, C. S.; Wuttke, S. The Current Status of MOF and COF Applications. *Angewandte Chemie International Edition* **2021**, *60* (45), 23975–24001. <https://doi.org/10.1002/anie.202106259>.
- (16) Campbell, M.; Dincă, M. Metal–Organic Frameworks as Active Materials in Electronic Sensor Devices. *Sensors* **2017**, *17* (5), 1108. <https://doi.org/10.3390/s17051108>.
- (17) Zhao, P.; Tsang, S. C. E.; Fairen-Jimenez, D. Structural Heterogeneity and Dynamics in Flexible Metal–Organic Frameworks. *Cell Rep Phys Sci* **2021**, *2* (9), 100544. <https://doi.org/10.1016/j.xcrp.2021.100544>.
- (18) Li, X.; Sensharma, D.; Loots, L.; Geng, S.; Nikkhah, S. J.; Lin, E.; Bon, V.; Liu, W.; Wang, Z.; He, T.; Mukherjee, S.; Vandichel, M.; Kaskel, S.; Barbour, L. J.; Zhang, Z.; Zaworotko, M. J. Reversible Phase Transformations in a Double-Walled Diamondoid Coordination Network with a

- Stepped Isotherm for Methane. *J Am Chem Soc* **2024**, *146* (27), 18387–18395. <https://doi.org/10.1021/jacs.4c03555>.
- (19) Wang, S.-Q.; Mukherjee, S.; Zaworotko, M. J. Spiers Memorial Lecture: Coordination Networks That Switch between Nonporous and Porous Structures: An Emerging Class of Soft Porous Crystals. *Faraday Discuss* **2021**, *231*, 9–50. <https://doi.org/10.1039/D1FD00037C>.
- (20) Schneemann, A.; Bon, V.; Schwedler, I.; Senkovska, I.; Kaskel, S.; Fischer, R. A. Flexible Metal–Organic Frameworks. *Chem. Soc. Rev.* **2014**, *43* (16), 6062–6096. <https://doi.org/10.1039/C4CS00101J>.
- (21) Jeong, S.; Kim, D.; Park, J.; Shin, S.; Kim, H.; Jeong, H.; Moon, D.; Moon, H. R.; Lah, M. S. *Topology Conversions of Non-Interpenetrated Metal-Organic Frameworks to Doubly Interpenetrated Metal-Organic Frameworks*; 2017. <http://pubs.acs.org>.
- (22) Widmer, R. N.; Lampronti, G. I.; Chibani, S.; Wilson, C. W.; Anzellini, S.; Farsang, S.; Kleppe, A. K.; Casati, N. P. M.; MacLeod, S. G.; Redfern, S. A. T.; Coudert, F.-X.; Bennett, T. D. Rich Polymorphism of a Metal–Organic Framework in Pressure–Temperature Space. *J Am Chem Soc* **2019**, *141* (23), 9330–9337. <https://doi.org/10.1021/jacs.9b03234>.
- (23) Spencer, E. C.; Angel, R. J.; Ross, N. L.; Hanson, B. E.; Howard, J. A. K. Pressure-Induced Cooperative Bond Rearrangement in a Zinc Imidazolate Framework: A High-Pressure Single-Crystal X-Ray Diffraction Study. *J Am Chem Soc* **2009**, *131* (11), 4022–4026. <https://doi.org/10.1021/ja808531m>.
- (24) Zheng, Z.; Rong, Z.; Nguyen, H. L.; Yaghi, O. M. Structural Chemistry of Zeolitic Imidazolate Frameworks. *Inorg Chem* **2023**, *62* (51), 20861–20873. <https://doi.org/10.1021/acs.inorgchem.3c02322>.
- (25) Wang, H.; Pei, X.; Kalmutzki, M. J.; Yang, J.; Yaghi, O. M. Large Cages of Zeolitic Imidazolate Frameworks. *Acc Chem Res* **2022**, *55* (5), 707–721. <https://doi.org/10.1021/acs.accounts.1c00740>.
- (26) Jiang, H.; Jia, J.; Shkurenko, A.; Chen, Z.; Adil, K.; Belmabkhout, Y.; Weselinski, L. J.; Assen, A. H.; Xue, D.-X.; O’Keeffe, M.; Eddaoudi, M. Enriching the Reticular Chemistry Repertoire: Merged Nets Approach for the Rational Design of Intricate Mixed-Linker Metal–Organic Framework Platforms. *J Am Chem Soc* **2018**, *140* (28), 8858–8867. <https://doi.org/10.1021/jacs.8b04745>.
- (27) Park, K. S.; Ni, Z.; Côté, A. P.; Choi, J. Y.; Huang, R.; Uribe-Romo, F. J.; Chae, H. K.; O’Keeffe, M.; Yaghi, O. M. Exceptional Chemical and Thermal Stability of Zeolitic Imidazolate Frameworks. *Proceedings of the National Academy of Sciences* **2006**, *103* (27), 10186–10191. <https://doi.org/10.1073/pnas.0602439103>.
- (28) Tian, Y.; Cai, C.; Ji, Y.; You, X.; Peng, S.; Lee, G. [Co₅(Im)₁₀·2 MB]_∞: A Metal–Organic Open-Framework with Zeolite-Like Topology. *Angewandte Chemie International Edition* **2002**, *41* (8), 1384–1386. [https://doi.org/10.1002/1521-3773\(20020415\)41:8<1384::AID-ANIE1384>3.0.CO;2-6](https://doi.org/10.1002/1521-3773(20020415)41:8<1384::AID-ANIE1384>3.0.CO;2-6).
- (29) Tian, Y.; Cai, C.; Ren, X.; Duan, C.; Xu, Y.; Gao, S.; You, X. The Silica-Like Extended Polymorphism of Cobalt(II) Imidazolate Three-Dimensional Frameworks: X-ray Single-Crystal Structures and Magnetic Properties. *Chemistry – A European Journal* **2003**, *9* (22), 5673–5685. <https://doi.org/10.1002/chem.200304957>.

- (30) Rettig, S. J.; Storr, A.; Summers, D. A.; Thompson, R. C.; Trotter, J. Iron(II) 2-Methylimidazolate and Copper(II) 1,2,4-Triazolate Complexes: Systems Exhibiting Long-Range Ferromagnetic Ordering at Low Temperatures. *Can J Chem* **1999**, *77* (4), 425–433. <https://doi.org/10.1139/v99-063>.
- (31) Huang, X.; Lin, Y.; Zhang, J.; Chen, X. Ligand-Directed Strategy for Zeolite-Type Metal–Organic Frameworks: Zinc(II) Imidazolates with Unusual Zeolitic Topologies. *Angewandte Chemie International Edition* **2006**, *45* (10), 1557–1559. <https://doi.org/10.1002/anie.200503778>.
- (32) Guo, S.; Li, H.-Z.; Wang, Z.-W.; Zhu, Z.-Y.; Zhang, S.-H.; Wang, F.; Zhang, J. Syntheses of New Zeolitic Imidazolate Frameworks in Dimethyl Sulfoxide. *Inorg Chem Front* **2022**, *9* (9), 2011–2015. <https://doi.org/10.1039/D1QI01538A>.
- (33) Baerlocher, C.; McCusker, L. B. *Database of Zeolite Structures*. <http://www.iza-structure.org/databases/> (accessed 2019-02-12).
- (34) O’Keeffe, M.; Peskov, M. A.; Ramsden, S. J.; Yaghi, O. M. The Reticular Chemistry Structure Resource (RCSR) Database of, and Symbols for, Crystal Nets. *Acc Chem Res* **2008**, *41* (12), 1782–1789. <https://doi.org/10.1021/ar800124u>.
- (35) Banerjee, R.; Phan, A.; Wang, B.; Knobler, C.; Furukawa, H.; O’Keeffe, M.; Yaghi, O. M. High-Throughput Synthesis of Zeolitic Imidazolate Frameworks and Application to CO₂ Capture. *Science (1979)* **2008**, *319* (5865), 939–943. <https://doi.org/10.1126/science.1152516>.
- (36) Bennett, T. D.; Cao, S.; Tan, J. C.; Keen, D. A.; Bithell, E. G.; Beldon, P. J.; Friscic, T.; Cheetham, A. K. Facile Mechanochemistry of Amorphous Zeolitic Imidazolate Frameworks. *J Am Chem Soc* **2011**, *133* (37), 14546–14549. <https://doi.org/10.1021/ja206082s>.
- (37) Bennett, T. D.; Keen, D. A.; Tan, J.; Barney, E. R.; Goodwin, A. L.; Cheetham, A. K. Thermal Amorphization of Zeolitic Imidazolate Frameworks. *Angewandte Chemie International Edition* **2011**, *50* (13), 3067–3071. <https://doi.org/10.1002/anie.201007303>.
- (38) Shaw, E. V.; Chester, A. M.; Robertson, G. P.; Castillo-Blas, C.; Bennett, T. D. Synthetic and Analytical Considerations for the Preparation of Amorphous Metal–Organic Frameworks. *Chem Sci* **2024**, *15* (28), 10689–10712. <https://doi.org/10.1039/D4SC01433B>.
- (39) Martins, G. A. V.; Byrne, P. J.; Allan, P.; Teat, S. J.; Slawin, A. M. Z.; Li, Y.; Morris, R. E. The Use of Ionic Liquids in the Synthesis of Zinc Imidazolate Frameworks. *Dalton Transactions* **2010**, *39* (7), 1758–1762. <https://doi.org/10.1039/b917348j>.
- (40) Lanchas, M.; Vallejo-Sánchez, D.; Beobide, G.; Castillo, O.; Aguayo, A. T.; Luque, A.; Román, P. A Direct Reaction Approach for the Synthesis of Zeolitic Imidazolate Frameworks: Template and Temperature Mediated Control on Network Topology and Crystal Size. *Chemical Communications* **2012**, *48* (79), 9930–9932. <https://doi.org/10.1039/c2cc34787c>.
- (41) Morris, W.; Leung, B.; Furukawa, H.; Yaghi, O. K.; He, N.; Hayashi, H.; Houndonougbo, Y.; Asta, M.; Laird, B. B.; Yaghi, O. M. A Combined Experimental–Computational Investigation of Carbon Dioxide Capture in a Series of Isorecticular Zeolitic Imidazolate Frameworks. *J Am Chem Soc* **2010**, *132* (32), 11006–11008. <https://doi.org/10.1021/ja104035j>.
- (42) Yang, J.; Zhang, Y.-B.; Liu, Q.; Trickett, C. A.; Gutiérrez-Puebla, E.; Monge, M. Á.; Cong, H.; Aldossary, A.; Deng, H.; Yaghi, O. M. Principles of Designing Extra-Large Pore Openings and

Cages in Zeolitic Imidazolate Frameworks. *J Am Chem Soc* **2017**, *139* (18), 6448–6455. <https://doi.org/10.1021/jacs.7b02272>.

- (43) Shi, Q.; Kang, X.; Shi, F.-N.; Dong, J. Zn₁₀(Im)₂₀·4DBF: An Unprecedented 10-Nodal Zeolitic Topology with a 10-MR Channel and 10 Crystallographically Independent Zn Atoms. *Chemical Communications* **2015**, *51* (6), 1131–1134. <https://doi.org/10.1039/C4CC07105K>.
- (44) Meng, Q.; Wang, J.; Shi, Q.; Dong, J. Synthesis of a New ATN-Type Zeolitic Imidazolate Framework through Cooperative Effects of *N,N*-Dipropylformamide and *n*-Butylamine. *CrystrEngComm* **2021**, *23* (19), 3429–3433. <https://doi.org/10.1039/D1CE00287B>.
- (45) Shi, Q.; Xu, W.-J.; Huang, R.-K.; Zhang, W.-X.; Li, Y.; Wang, P.; Shi, F.-N.; Li, L.; Li, J.; Dong, J. Zeolite CAN and AFI-Type Zeolitic Imidazolate Frameworks with Large 12-Membered Ring Pore Openings Synthesized Using Bulky Amides as Structure-Directing Agents. *J Am Chem Soc* **2016**, *138* (50), 16232–16235. <https://doi.org/10.1021/jacs.6b11197>.
- (46) Mu, K.; Wang, J.; Gao, M.; Wu, Y.; Shi, Q.; Dong, J. Template Role of Long Alkyl-Chain Amides in the Synthesis of Zeolitic Imidazolate Frameworks. *ACS Omega* **2024**, *9* (32), 34777–34786. <https://doi.org/10.1021/acsomega.4c04259>.
- (47) Tian, Y.; Zhao, Y.; Chen, Z.; Zhang, G.; Weng, L.; Zhao, D. Design and Generation of Extended Zeolitic Metal–Organic Frameworks (ZMOFs): Synthesis and Crystal Structures of Zinc(II) Imidazolate Polymers with Zeolitic Topologies. *Chemistry – A European Journal* **2007**, *13* (15), 4146–4154. <https://doi.org/10.1002/chem.200700181>.
- (48) Ramirez, J. R.; Yang, H.; Kane, C. M.; Ley, A. N.; Holman, K. T. Reproducible Synthesis and High Porosity of Mer-Zn(Im)₂ (ZIF-10): Exploitation of an Apparent Double-Eight Ring Template. *J Am Chem Soc* **2016**, *138* (37), 12017–12020. <https://doi.org/10.1021/jacs.6b06375>.
- (49) James, S. L.; Adams, C. J.; Bolm, C.; Braga, D.; Collier, P.; Friščić, T.; Grepioni, F.; Harris, K. D. M.; Hyett, G.; Jones, W.; Krebs, A.; Mack, J.; Maini, L.; Orpen, A. G.; Parkin, I. P.; Shearouse, W. C.; Steed, J. W.; Waddell, D. C. Mechanochemistry: Opportunities for New and Cleaner Synthesis. *Chem. Soc. Rev.* **2012**, *41* (1), 413–447. <https://doi.org/10.1039/C1CS15171A>.
- (50) Tan, D.; Loots, L.; Friščić, T. Towards Medicinal Mechanochemistry: Evolution of Milling from Pharmaceutical Solid Form Screening to the Synthesis of Active Pharmaceutical Ingredients (APIs). *Chemical Communications* **2016**, *52* (50), 7760–7781. <https://doi.org/10.1039/C6CC02015A>.
- (51) Do, J.-L.; Friščić, T. Mechanochemistry: A Force of Synthesis. *ACS Cent Sci* **2017**, *3* (1), 13–19. <https://doi.org/10.1021/acscentsci.6b00277>.
- (52) Solares-Briones, M.; Coyote-Dotor, G.; Páez-Franco, J. C.; Zermeño-Ortega, M. R.; de la O Contreras, C. M.; Canseco-González, D.; Avila-Sorrosa, A.; Morales-Morales, D.; Germán-Acacio, J. M. Mechanochemistry: A Green Approach in the Preparation of Pharmaceutical Cocrystals. *Pharmaceutics* **2021**, *13* (6), 790. <https://doi.org/10.3390/pharmaceutics13060790>.
- (53) Fantozzi, N.; Volle, J. N.; Porcheddu, A.; Virieux, D.; García, F.; Colacino, E. Green Metrics in Mechanochemistry. *Chemical Society Reviews*. Royal Society of Chemistry September 11, 2023, pp 6680–6714. <https://doi.org/10.1039/d2cs00997h>.
- (54) Bodach, A.; Portet, A.; Winkelmann, F.; Herrmann, B.; Gallou, F.; Ponnusamy, E.; Virieux, D.; Colacino, E.; Felderhoff, M. Scalability of Pharmaceutical Co-Crystal Formation by

- (55) Reynes, J. F.; Isoni, V.; García, F. Tinkering with Mechanochemical Tools for Scale Up. *Angewandte Chemie International Edition* **2023**, *62* (44).
<https://doi.org/10.1002/anie.202300819>.
- (56) Akimbekov, Z.; Katsenis, A. D.; Nagabhushana, G. P.; Ayoub, G.; Arhangel'skis, M.; Morris, A. J.; Frišćić, T.; Navrotsky, A. Experimental and Theoretical Evaluation of the Stability of True MOF Polymorphs Explains Their Mechanochemical Interconversions. *J Am Chem Soc* **2017**, *139* (23), 7952–7957. <https://doi.org/10.1021/jacs.7b03144>.
- (57) Mottillo, C.; Frišćić, T. Advances in Solid-State Transformations of Coordination Bonds: From the Ball Mill to the Aging Chamber. *Molecules* **2017**, *22* (1), 144.
<https://doi.org/10.3390/molecules22010144>.
- (58) Julien, P. A.; Mottillo, C.; Frišćić, T. Metal–Organic Frameworks Meet Scalable and Sustainable Synthesis. *Green Chemistry* **2017**, *19* (12), 2729–2747. <https://doi.org/10.1039/C7GC01078H>.
- (59) Frišćić, T.; Mottillo, C.; Titi, H. M. Mechanochemistry for Synthesis. *Angewandte Chemie International Edition* **2020**, *59* (3), 1018–1029. <https://doi.org/10.1002/anie.201906755>.
- (60) Stolar, T.; Užarević, K. Mechanochemistry: An Efficient and Versatile Toolbox for Synthesis, Transformation, and Functionalization of Porous Metal–Organic Frameworks. *CrystEngComm* **2020**, *22* (27), 4511–4525. <https://doi.org/10.1039/D0CE00091D>.
- (61) Reynes, J. F.; Leon, F.; García, F. Mechanochemistry for Organic and Inorganic Synthesis. *ACS Organic and Inorganic Au*. American Chemical Society October 2, 2024.
<https://doi.org/10.1021/acsorginorgau.4c00001>.
- (62) Tanaka, S.; Kida, K.; Nagaoka, T.; Ota, T.; Miyake, Y. Mechanochemical Dry Conversion of Zinc Oxide to Zeolitic Imidazolate Framework. *Chemical Communications* **2013**, *49* (72), 7884.
<https://doi.org/10.1039/c3cc43028f>.
- (63) Beldon, P. J.; Fábíán, L.; Stein, R. S.; Thirumurugan, A.; Cheetham, A. K.; Frišćić, T. Rapid Room-Temperature Synthesis of Zeolitic Imidazolate Frameworks by Using Mechanochemistry. *Angewandte Chemie International Edition* **2010**, *49* (50), 9640–9643.
<https://doi.org/10.1002/anie.201005547>.
- (64) Cliffe, M. J.; Mottillo, C.; Stein, R. S.; Bučar, D.-K.; Frišćić, T. Accelerated Aging: A Low Energy, Solvent-Free Alternative to Solvothermal and Mechanochemical Synthesis of Metal–Organic Materials. *Chem Sci* **2012**, *3* (8), 2495–2500. <https://doi.org/10.1039/C2SC20344H>.
- (65) Mottillo, C.; Lu, Y.; Pham, M.-H.; Cliffe, M. J.; Do, T.-O.; Frišćić, T. Mineral Neogenesis as an Inspiration for Mild, Solvent-Free Synthesis of Bulk Microporous Metal–Organic Frameworks from Metal (Zn, Co) Oxides. *Green Chemistry* **2013**, *15* (8), 2121.
<https://doi.org/10.1039/c3gc40520f>.
- (66) Gugin, N.; Villajos, J. A.; Feldmann, I.; Emmerling, F. Mix and Wait – a Relaxed Way for Synthesizing ZIF-8. *RSC Adv* **2022**, *12* (15), 8940–8944. <https://doi.org/10.1039/D2RA00740A>.
- (67) Michalchuk, A. A. L.; Emmerling, F. Time-Resolved In Situ Monitoring of Mechanochemical Reactions. *Angewandte Chemie International Edition* **2022**, *61* (21).
<https://doi.org/10.1002/anie.202117270>.

- (68) Batzdorf, L.; Fischer, F.; Wilke, M.; Wenzel, K. J.; Emmerling, F. Direct in Situ Investigation of Milling Reactions Using Combined X-Ray Diffraction and Raman Spectroscopy. *Angewandte Chemie - International Edition* **2015**, *54* (6), 1799–1802. <https://doi.org/10.1002/anie.201409834>.
- (69) Brekalo, I.; Yuan, W.; Mottillo, C.; Lu, Y.; Zhang, Y.; Casaban, J.; Holman, K. T.; James, S. L.; Duarte, F.; Williams, P. A.; Harris, K. D. M.; Friščić, T. Manometric Real-Time Studies of the Mechanochemical Synthesis of Zeolitic Imidazolate Frameworks. *Chem Sci* **2020**, *11* (8), 2141–2147. <https://doi.org/10.1039/C9SC05514B>.
- (70) Ma, X.; Yuan, W.; Bell, S. E. J.; James, S. L. Better Understanding of Mechanochemical Reactions: Raman Monitoring Reveals Surprisingly Simple ‘Pseudo-Fluid’ Model for a Ball Milling Reaction. *Chemical Communications* **2014**, *50* (13), 1585. <https://doi.org/10.1039/c3cc47898j>.
- (71) Friščić, T.; Halasz, I.; Beldon, P. J.; Belenguer, A. M.; Adams, F.; Kimber, S. A. J.; Honkimäki, V.; Dinnebier, R. E. Real-Time and in Situ Monitoring of Mechanochemical Milling Reactions. *Nat Chem* **2013**, *5* (1), 66–73. <https://doi.org/10.1038/nchem.1505>.
- (72) Katsenis, A. D.; Puškarić, A.; Štrukil, V.; Mottillo, C.; Julien, P. A.; Užarević, K.; Pham, M.-H.; Do, T.-O.; Kimber, S. A. J.; Lazić, P.; Magdysyuk, O.; Dinnebier, R. E.; Halasz, I.; Friščić, T. In Situ X-Ray Diffraction Monitoring of a Mechanochemical Reaction Reveals a Unique Topology Metal-Organic Framework. *Nat Commun* **2015**, *6* (1), 6662. <https://doi.org/10.1038/ncomms7662>.
- (73) Crawford, D.; Casaban, J.; Haydon, R.; Giri, N.; McNally, T.; James, S. L. Synthesis by Extrusion: Continuous, Large-Scale Preparation of MOFs Using Little or No Solvent. *Chem Sci* **2015**, *6* (3), 1645–1649. <https://doi.org/10.1039/C4SC03217A>.
- (74) Crawford, D. E.; Casaban, J. Recent Developments in Mechanochemical Materials Synthesis by Extrusion. *Advanced Materials* **2016**, *28* (27), 5747–5754. <https://doi.org/10.1002/adma.201505352>.
- (75) Novendra, N.; Marrett, J. M.; Katsenis, A. D.; Titi, H. M.; Arhangelskis, M.; Friščić, T.; Navrotsky, A. Linker Substituents Control the Thermodynamic Stability in Metal-Organic Frameworks. *J Am Chem Soc* **2020**, *142* (52), 21720–21729. <https://doi.org/10.1021/jacs.0c09284>.
- (76) Arhangelskis, M.; Katsenis, A. D.; Novendra, N.; Akimbekov, Z.; Gandrath, D.; Marrett, J. M.; Ayoub, G.; Morris, A. J.; Farha, O. K.; Friščić, T.; Navrotsky, A. Theoretical Prediction and Experimental Evaluation of Topological Landscape and Thermodynamic Stability of a Fluorinated Zeolitic Imidazolate Framework. *Chemistry of Materials* **2019**, *31* (10), 3777–3783. <https://doi.org/10.1021/acs.chemmater.9b00994>.
- (77) Xu, Y.; Marrett, J. M.; Titi, H. M.; Darby, J. P.; Morris, A. J.; Friščić, T.; Arhangelskis, M. Experimentally Validated Ab Initio Crystal Structure Prediction of Novel Metal–Organic Framework Materials. *J Am Chem Soc* **2023**, *145* (6), 3515–3525. <https://doi.org/10.1021/jacs.2c12095>.
- (78) Moran, J. R.; Karbach, S.; Cram, D. J. Cavitanids: Synthetic Molecular Vessels. *J Am Chem Soc* **1982**, *104* (21), 5826–5828. <https://doi.org/10.1021/ja00385a064>.
- (79) Brekalo, I.; Kane, C. M.; Ley, A. N.; Ramirez, J. R.; Friščić, T.; Holman, K. T. Use of a “Shoe-Last” Solid-State Template in the Mechanochemical Synthesis of High-Porosity RHO-Zinc Imidazolate. *J Am Chem Soc* **2018**, *140* (32), 10104–10108. <https://doi.org/10.1021/jacs.8b05471>.

- (80) Brekalo, I.; Deliz, D. E.; Kane, C. M.; Frišćić, T.; Holman, K. T. Exploring the Scope of Macrocyclic “Shoe-Last” Templates in the Mechanochemical Synthesis of RHO Topology Zeolitic Imidazolate Frameworks (ZIFs). *Molecules* **2020**, *25* (3), 633. <https://doi.org/10.3390/molecules25030633>.
- (81) Wenger, L. E.; Hanusa, T. P. Synthesis without Solvent: Consequences for Mechanochemical Reactivity. *Chemical Communications* **2023**, *59* (96), 14210–14222. <https://doi.org/10.1039/d3cc04929a>.
- (82) Strobridge, F. C.; Judaš, N.; Frišćić, T. A Stepwise Mechanism and the Role of Water in the Liquid-Assisted Grinding Synthesis of Metal–Organic Materials. *CrystEngComm* **2010**, *12* (8), 2409. <https://doi.org/10.1039/c003521a>.
- (83) Stolar, T.; Batzdorf, L.; Lukin, S.; Žilić, D.; Motillo, C.; Frišćić, T.; Emmerling, F.; Halasz, I.; Užarević, K. In Situ Monitoring of the Mechanochemical Synthesis of the Archetypal Metal–Organic Framework HKUST-1: Effect of Liquid Additives on the Milling Reactivity. *Inorg Chem* **2017**, *56* (11), 6599–6608. <https://doi.org/10.1021/acs.inorgchem.7b00707>.
- (84) Fidelli, A. M.; Karadeniz, B.; Howarth, A. J.; Huskić, I.; Germann, L. S.; Halasz, I.; Etter, M.; Moon, S. Y.; Dinnebier, R. E.; Stilinović, V.; Farha, O. K.; Frišćić, T.; Užarević, K. Green and Rapid Mechanochemical Synthesis of High-Porosity NU- and UiO-Type Metal–Organic Frameworks. *Chemical Communications* **2018**, *54* (51), 6999–7002. <https://doi.org/10.1039/c8cc03189d>.
- (85) Groom, C. R.; Bruno, I. J.; Lightfoot, M. P.; Ward, S. C. The Cambridge Structural Database. *Acta Crystallogr B Struct Sci Cryst Eng Mater* **2016**, *72* (2), 171–179. <https://doi.org/10.1107/S2052520616003954>.
- (86) Schröder, C. A.; Saha, S.; Huber, K.; Leoni, S.; Wiebcke, M. Metastable Metal Imidazolates: Development of Targeted Syntheses by Combining Experimental and Theoretical Investigations of the Formation Mechanisms. *Z Kristallogr Cryst Mater* **2014**, *229* (12), 807–822. <https://doi.org/10.1515/zkri-2014-1788>.
- (87) Spencer, E. C.; Angel, R. J.; Ross, N. L.; Hanson, B. E.; Howard, J. A. K. Pressure-Induced Cooperative Bond Rearrangement in a Zinc Imidazolate Framework: A High-Pressure Single-Crystal X-Ray Diffraction Study. *J Am Chem Soc* **2009**, *131* (11), 4022–4026. <https://doi.org/10.1021/ja808531m>.
- (88) Schröder, C. A.; Baburin, I. A.; van Wüllen, L.; Wiebcke, M.; Leoni, S. Subtle Polymorphism of Zinc Imidazolate Frameworks: Temperature-Dependent Ground States in the Energy Landscape Revealed by Experiment and Theory. *CrystEngComm* **2013**, *15* (20), 4036–4040. <https://doi.org/10.1039/C2CE26045J>.
- (89) Blatov, V. A.; Shevchenko, A. P.; Proserpio, D. M. Applied Topological Analysis of Crystal Structures with the Program Package ToposPro. *Cryst Growth Des* **2014**, *14* (7), 3576–3586. <https://doi.org/10.1021/cg500498k>.
- (90) Shevchenko, A. P.; Shabalin, A. A.; Karpukhin, I. Yu.; Blatov, V. A. Topological Representations of Crystal Structures: Generation, Analysis and Implementation in the *TopCryst* System. *Science and Technology of Advanced Materials: Methods* **2022**, *2* (1), 250–265. <https://doi.org/10.1080/27660400.2022.2088041>.
- (91) Wu, X.; Yue, H.; Zhang, Y.; Gao, X.; Li, X.; Wang, L.; Cao, Y.; Hou, M.; An, H.; Zhang, L.; Li, S.; Ma, J.; Lin, H.; Fu, Y.; Gu, H.; Lou, W.; Wei, W.; Zare, R. N.; Ge, J. Packaging and

Delivering Enzymes by Amorphous Metal-Organic Frameworks. *Nat Commun* **2019**, *10* (1), 5165. <https://doi.org/10.1038/s41467-019-13153-x>.

- (92) Cao, S.; Bennett, T. D.; Keen, D. A.; Goodwin, A. L.; Cheetham, A. K. Amorphization of the Prototypical Zeolitic Imidazolate Framework ZIF-8 by Ball-Milling. *Chemical Communications* **2012**, *48* (63), 7805. <https://doi.org/10.1039/c2cc33773h>.
- (93) Bennett, T. D.; Saines, P. J.; Keen, D. A.; Tan, J.; Cheetham, A. K. Ball-Milling-Induced Amorphization of Zeolitic Imidazolate Frameworks (ZIFs) for the Irreversible Trapping of Iodine. *Chemistry – A European Journal* **2013**, *19* (22), 7049–7055. <https://doi.org/10.1002/chem.201300216>.
- (94) Bennett, T. D.; Horike, S. Liquid, Glass and Amorphous Solid States of Coordination Polymers and Metal–Organic Frameworks. *Nat Rev Mater* **2018**, *3* (11), 431–440. <https://doi.org/10.1038/s41578-018-0054-3>.
- (95) Galvelis, R.; Slater, B.; Cheetham, A. K.; Mellot-Draznieks, C. Comparison of the Relative Stability of Zinc and Lithium-Boron Zeolitic Imidazolate Frameworks. *CrystEngComm* **2012**, *14* (2), 374–378. <https://doi.org/10.1039/C1CE05854A>.
- (96) Mellot-Draznieks, C.; Kerkeni, B. Exploring the Interplay between Ligand and Topology in Zeolitic Imidazolate Frameworks with Computational Chemistry. *Mol Simul* **2014**, *40* (1–3), 25–32. <https://doi.org/10.1080/08927022.2013.845298>.
- (97) Lewis, D. W.; Ruiz-Salvador, A. R.; Gómez, A.; Rodriguez-Albelo, L. M.; Coudert, F.-X.; Slater, B.; Cheetham, A. K.; Mellot-Draznieks, C. Zeolitic Imidazole Frameworks: Structural and Energetics Trends Compared with Their Zeolite Analogues. *CrystEngComm* **2009**, *11* (11), 2272. <https://doi.org/10.1039/b912997a>.
- (98) Baburin, I. A.; Leoni, S.; Seifert, G. Enumeration of Not-Yet-Synthesized Zeolitic Zinc Imidazolate MOF Networks: A Topological and DFT Approach. *J Phys Chem B* **2008**, *112* (31), 9437–9443. <https://doi.org/10.1021/jp801681w>.
- (99) Lee, S.; Nam, D.; Yang, D. C.; Choe, W. Unveiling Hidden Zeolitic Imidazolate Frameworks Guided by Intuition-Based Geometrical Factors. *Small* **2023**, *19* (15). <https://doi.org/10.1002/sml.202300036>.
- (100) Perdew, J. P.; Burke, K.; Ernzerhof, M. Generalized Gradient Approximation Made Simple. *Phys Rev Lett* **1996**, *77* (18), 3865–3868. <https://doi.org/10.1103/PhysRevLett.77.3865>.
- (101) Grimme, S. Semiempirical GGA-type Density Functional Constructed with a Long-range Dispersion Correction. *J Comput Chem* **2006**, *27* (15), 1787–1799. <https://doi.org/10.1002/jcc.20495>.
- (102) Grimme, S.; Antony, J.; Ehrlich, S.; Krieg, H. A Consistent and Accurate Ab Initio Parametrization of Density Functional Dispersion Correction (DFT-D) for the 94 Elements H-Pu. *J Chem Phys* **2010**, *132* (15). <https://doi.org/10.1063/1.3382344>.
- (103) Leonel, G. J.; Lennox, C. B.; Xu, Y.; Arhangelskis, M.; Friščić, T.; Navrotsky, A. Experimental and Theoretical Evaluation of the Thermodynamics of the Carbonation Reaction of ZIF-8 and Its Close-Packed Polymorph with Carbon Dioxide. *The Journal of Physical Chemistry C* **2023**, *127* (39), 19520–19526. <https://doi.org/10.1021/acs.jpcc.3c04135>.

- (104) Clark, S. J.; Segall, M. D.; Pickard, C. J.; Hasnip, P. J.; Probert, M. I. J.; Refson, K.; Payne, M. C. First Principles Methods Using CASTEP. *Z Kristallogr Cryst Mater* **2005**, *220* (5–6), 567–570. <https://doi.org/10.1524/zkri.220.5.567.65075>.
- (105) Pulido, A.; Chen, L.; Kaczorowski, T.; Holden, D.; Little, M. A.; Chong, S. Y.; Slater, B. J.; McMahon, D. P.; Bonillo, B.; Stackhouse, C. J.; Stephenson, A.; Kane, C. M.; Clowes, R.; Hasell, T.; Cooper, A. I.; Day, G. M. Functional Materials Discovery Using Energy–Structure–Function Maps. *Nature* **2017**, *543* (7647), 657–664. <https://doi.org/10.1038/nature21419>.
- (106) Hasa, D.; Pastore, M.; Arhangel'skis, M.; Gabriele, B.; Cruz-Cabeza, A. J.; Rauber, G. S.; Bond, A. D.; Jones, W. On the Kinetics of Solvate Formation through Mechanochemistry. *CrystEngComm* **2019**, *21* (13), 2097–2104. <https://doi.org/10.1039/C8CE00871J>.
- (107) Sheldrick, G. M. A Short History of SHELX. *Acta Crystallogr A* **2008**, *64* (1), 112–122. <https://doi.org/10.1107/S0108767307043930>.
- (108) Sheldrick, G. M. Crystal Structure Refinement with SHELXL. *Acta Crystallogr C Struct Chem* **2015**, *71* (1), 3–8. <https://doi.org/10.1107/S2053229614024218>.
- (109) Boulton, A.; Louër, D. Powder Pattern Indexing with the Dichotomy Method. *J Appl Crystallogr* **2004**, *37* (5), 724–731. <https://doi.org/10.1107/S0021889804014876>.
- (110) Altomare, A.; Giacovazzo, C.; Guagliardi, A.; Moliterni, A. G. G.; Rizzi, R.; Werner, P.-E. New Techniques for Indexing: N-TREOR in EXPO. *J Appl Crystallogr* **2000**, *33* (4), 1180–1186. <https://doi.org/10.1107/S0021889800006427>.
- (111) Altomare, A.; Cuocci, C.; Giacovazzo, C.; Moliterni, A.; Rizzi, R.; Corriero, N.; Falcicchio, A. EXPO2013: A Kit of Tools for Phasing Crystal Structures from Powder Data. *J Appl Crystallogr* **2013**, *46* (4), 1231–1235. <https://doi.org/10.1107/S0021889813013113>.
- (112) Le Bail, A.; Duroy, H.; Fourquet, J. L. Ab-Initio Structure Determination of LiSbWO₆ by X-Ray Powder Diffraction. *Mater Res Bull* **1988**, *23* (3), 447–452. [https://doi.org/10.1016/0025-5408\(88\)90019-0](https://doi.org/10.1016/0025-5408(88)90019-0).
- (113) Coelho, A. A. TOPAS and TOPAS-Academic: An Optimization Program Integrating Computer Algebra and Crystallographic Objects Written in C++. *J Appl Crystallogr* **2018**, *51* (1), 210–218. <https://doi.org/10.1107/S1600576718000183>.
- (114) Aminoff, G. XXIV. Über Lauephotogramme Und Struktur von Zinkit. *Z Kristallogr Cryst Mater* **1921**, *56* (1–6), 495–505. <https://doi.org/10.1524/zkri.1921.56.1.495>.
- (115) Barbour, L. J. X-Seed — A Software Tool for Supramolecular Crystallography. *Journal of Supramolecular Chemistry* **2001**, *1* (4–6), 189–191. [https://doi.org/10.1016/S1472-7862\(02\)00030-8](https://doi.org/10.1016/S1472-7862(02)00030-8).
- (116) Björkman, T. CIF2Cell: Generating Geometries for Electronic Structure Programs. *Comput Phys Commun* **2011**, *182* (5), 1183–1186. <https://doi.org/10.1016/j.cpc.2011.01.013>.